Article

Immunity

IL-9 signaling redirects CAR T cell fate toward CD8$^+$ memory and CD4$^+$ cycling states, enhancing antitumor efficacy

Graphical abstract

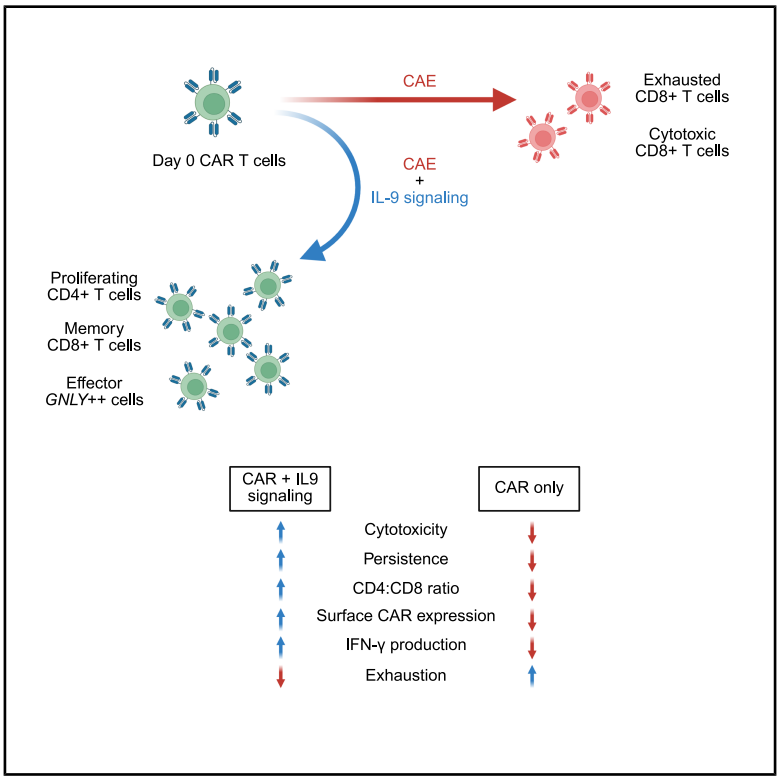

Highlights

- Engineering CAR T cells with IL-9 signaling boosts efficacy against solid tumors
- IL-9-signaling CD4$^+$ CAR T cells have increased Th1 and proliferative phenotypes
- Single-cell profiling reveals that IL-9 redirects CD8$^+$ T cell fate away from dysfunction
- IL-9-induced STAT1/STAT4 activation contributes to improved CAR T cell function

Authors

Sofía Castelli, Wesley V. Wilson, Ugur Uslu, ..., M. Angela Aznar, Regina M. Young, Carl H. June

Correspondence

ryoung@upenn.edu (R.M.Y.), cjune@upenn.edu (C.H.J.)

In brief

Castelli et al. show that incorporating interleukin-9 (IL-9) signaling reprograms chimeric antigen receptor (CAR) T cells to expand, persist, and resist dysfunction in solid tumors. This strategy improves antitumor activity at lower doses, suggesting a promising way to enhance the effectiveness of CAR T cell therapies against solid cancers.

Castelli et al., 2026, Immunity *59*, 195–212
January 13, 2026
https://doi.org/10.1016/j.immuni.2025.10.021

CellPress

Immunity

CellPress

Article

IL-9 signaling redirects CAR T cell fate toward CD8$^+$ memory and CD4$^+$ cycling states, enhancing antitumor efficacy

Sofía Castelli,[1,2] Wesley V. Wilson,[1,2] Ugur Uslu,[1,2] Amanda V. Finck,[1,2] Philipp C. Rommel,[1,2] Charles-Antoine Assenmacher,[3] Sebastian J. Atoche,[1,2] Mikko Siurala,[1,2] M. Angela Aznar,[1,2] Regina M. Young,[1,2,4,*] and Carl H. June[1,2,4,5,*]

[1]Center for Cellular Immunotherapies, Department of Pathology and Laboratory Medicine, University of Pennsylvania Perelman School of Medicine, Philadelphia, PA 19104, USA

[2]Parker Institute for Cancer Immunotherapy, University of Pennsylvania, Philadelphia, PA 19104, USA

[3]Comparative Pathology Core, Department of Pathobiology, School of Veterinary Medicine, University of Pennsylvania, Philadelphia, PA 19104, USA

[4]These authors contributed equally

[5]Lead contact

*Correspondence: ryoung@upenn.edu (R.M.Y.), cjune@upenn.edu (C.H.J.)

https://doi.org/10.1016/j.immuni.2025.10.021

SUMMARY

The success of chimeric antigen receptor (CAR) T cell therapies targeting solid tumors is limited by the immunosuppressive tumor microenvironment. We demonstrate that endowing CAR T cells with ectopic interleukin (IL)-9 signaling by co-expressing an IL-9 receptor rewires CAR T cell fate under antigen stress to enhance antitumor efficacy. In preclinical solid tumor models, IL-9-signaling CAR T cells exhibit increased expansion, persistence, and tumor infiltration, resulting in superior tumor control at substantially lower doses than conventional products. Trajectory and RNA velocity analyses of single-cell RNA sequencing data reveal that IL-9 signaling alters CAR T cell differentiation under antigen stress away from dysfunction, favoring a multipotent transition toward CD8$^+$ T cell memory and effector states and promoting a CD4$^+$ cell proliferative state. Interrogation of transcription factor pathways indicates that IL-9-mediated activation of STAT1 and STAT4 may contribute to the superior phenotype of IL-9-signaling CAR T cells, providing a promising therapeutic strategy for targeting solid cancers.

INTRODUCTION

Chimeric antigen receptor (CAR) T cell therapy has revolutionized the treatment of hematologic malignancies.[1,2] However, its efficacy against solid tumors is hindered by challenges such as limited T cell trafficking and infiltration, an immunosuppressive tumor microenvironment (TME), and on-target off-tumor toxicity.[3] Enhancing CAR T cell fitness is crucial to overcome these barriers.

Engineering CAR T cells to incorporate cytokine signaling pathways has shown both promise and challenges in addressing these obstacles.[4] For example, interleukin-2 (IL-2) supports T cell proliferation and survival but can cause severe adverse effects when administered systemically due to widespread receptor expression.[5–7] To mitigate these effects, strategies such as orthogonal IL-2 receptor-ligand pairs are under investigation (NCT05665062). Similarly, addition of IL-15 or IL-12 enhances CAR T cell antitumor efficacy in preclinical studies[8,9] but can increase the risk of toxicities when systemically administered to patients (NCT05103631)[10] (NCT02498912 and NCT06343376)[11,12] due to the broad expression of cytokine receptors, underscoring the need for safer strategies.[11,12]

Incorporating IL-9 signaling into CAR T cells represents a strategy for overcoming these barriers. IL-9, a common gamma chain (γ_c) cytokine, exerts diverse effects on tumor immunity, including enhanced immune cell recruitment and modulation, yet remains underexplored.[13–17] Notably, unlike receptors for other γ_c cytokines such as IL-2 and IL-15, the IL-9 receptor (IL-9R) has minimal expression in T cells and across normal tissues (Jiang et al.[18]). This unique expression profile minimizes toxicity risks, positioning IL-9-engineered CAR T cells as a safer and potentially more effective therapeutic alternative.

Our prior work demonstrated that CAR T cells engineered with an orthogonal IL-9 receptor (o9R) could effectively enhance antitumor immunity in murine solid tumor models.[19] However, emerging evidence suggests that the native IL-9R may confer distinct advantages over its orthogonal counterpart (Jiang et al.[18]). Here, we engineered CAR T cells to express an authentic IL-9R (CAR-IL9R T cells), enabling IL-9 responsiveness. By leveraging the intrinsic advantages of the native IL-9R, our work

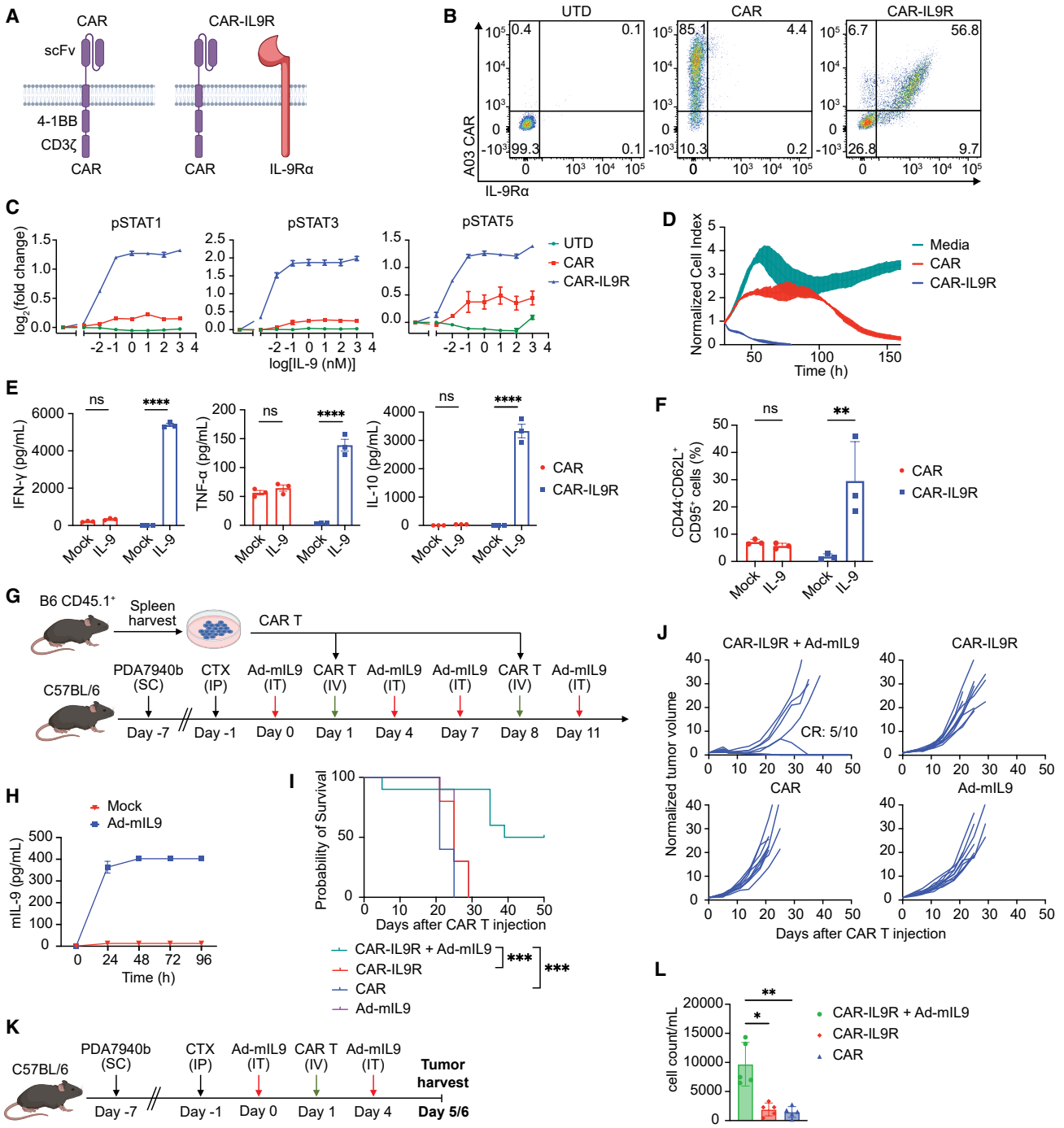

Figure 1. Authentic IL-9 signaling enhances CAR T cell antitumor efficacy in a syngeneic PDAC model

(A) Schematic representation of T cells transduced to express either CAR alone (CAR) or CAR and IL-9R (CAR-IL9R).

(B) Flow cytometric analysis of transduction efficiency in murine untransduced (UTD), CAR, or CAR-IL9R T cells.

(C) Quantification of phosphorylated STAT1 (pSTAT1), STAT3 (pSTAT3), and STAT5 (pSTAT5) in UTD, CAR, or CAR-IL9R T cells following 20-min IL-9 stimulation. Data are shown as log fold change of mean fluorescence intensity relative to non-stimulated samples. $n = 3$ biological replicates.

(D) *In vitro* cytotoxicity assay of PDA7940b tumor cells co-cultured with CAR or CAR-IL9R T cells (3:1 E:T ratio), with T cells pre-incubated with IL-9 for 48 h. Media was used as a control. $n = 3$.

(E) Cytokine secretion profiles of CAR and CAR-IL9R T cells, either untreated (mock) or pre-incubated with IL-9 for 48 h. $n = 3$ biological replicates.

(F) Bar graph showing the percentage of $CD44^{-}CD62L^{+}CD95^{+}$ cells in CAR or CAR-IL9R T cells, either untreated (mock) or treated with IL-9 for 48 h, as determined by flow cytometry. $n = 3$ biological replicates.

(G) Experimental design schematic for the syngeneic PDAC model. CTX, cyclophosphamide; s.c., subcutaneous; i.p., intraperitoneal; IT, intratumoral; and i.v., intravenous.

(legend continued on next page)

examines its unique contributions to human CAR T cell function, aiming to enhance the efficacy and precision of CAR T cell therapies for solid tumors.

RESULTS

Authentic IL-9 signaling enhances CAR T cell antitumor efficacy in a syngeneic PDAC model

To investigate how the introduction of authentic IL-9 signaling impacts cell extrinsic and intrinsic mechanisms governing CAR T cell function, we first employed a murine syngeneic PDAC model. Mouse T cells were engineered to express a mesothelin-targeted CAR (A03 CAR) and the wild-type IL-9R (CAR-IL9R T cells) (Figures 1A and 1B). IL-9 treatment resulted in the dose-dependent phosphorylation of signal transducer and activator of transcription 1 (STAT1), STAT3, and STAT5, consistent with known IL-9R signaling pathways (Figure 1C).[20] *In vitro* functional assays revealed that IL-9-treated CAR-IL9R T cells more effectively killed mesothelin-expressing PDA7940b cells, derived from KPC ($Kras^{LSL.G12D/+}p53^{R172H/+}$) mice, than control CAR T cells (Figure 1D). This enhancement was associated with increased production of cytokines, including interferon (IFN)-γ, tumor necrosis factor alpha (TNF-α), and IL-10 (Figure 1E). IL-9 did not induce cytokine production in control CAR T cells; however, elevated basal TNF-α levels were observed in both mock and IL-9-treated control CAR T cells, possibly due to tonic CAR signaling and known variability in baseline TNF-α expression.[21] Additionally, IL-9 treatment induced a shift toward a stem-like memory T cell phenotype ($CD44^{-}CD62L^{+}CD95^{+}$) in CAR-IL9R T cells (Figures 1F and S1A), mirroring findings from our previous studies with o9R-engineered T cells.[19]

Next, we evaluated the influence of the TME on the antitumor efficacy of CAR-IL9R T cells *in vivo* (Figure 1G). C57BL/6 mice were implanted subcutaneously with PDA7940b cells. T cells harvested from $CD45.1^{+}$ B6.SJL-$Ptprc^{a}$ $Pepc^{b}$/BoyJ mice were subjected to retroviral transduction to produce CAR-IL9R T cells. CAR and IL-9R transduction efficiency was confirmed by flow cytometry before intravenous (i.v.) injection into recipient mice. IL-9 was delivered via intratumoral injection of a replication-deficient adenovirus encoding murine IL-9 (Ad-mIL9) to ensure localized and transient cytokine expression within the TME. This strategy allowed for controlled ligand delivery without the need to further engineer the CAR T cells and reflects a clinically relevant approach, as intratumoral viral therapies are currently being evaluated in solid tumor trials (NCT03866525 and NCT02562755). Prior to *in vivo* testing, IL-9 production by tumor cells after Ad-mIL9 infection was validated *in vitro* (Figure 1H). Control groups for *in vivo* studies included mice treated with CAR-IL9R T cells alone, CAR T cells alone, or Ad-mIL9 alone. Treatment with CAR-IL9R + Ad-mIL9 significantly improved overall survival (Figure 1I) and reduced tumor progression (Figure 1J). Toxicity characterized by clinical signs of immune-effector-cell-associated neurotoxicity syndrome (ICANS) was observed in 1/10 mice treated with CAR-IL9R + Ad-mIL9. This phenomenon was observed at higher levels (5/12 mice) following treatment with CAR T cells expressing o9R and was investigated in our previous study.[19] Briefly, results suggested that toxicity was driven by CAR on-target off-tumor activity due to the expression of mesothelin in the murine but not healthy human meningeal layers.[19,22] An additional replicate of this experiment confirmed that IL-9 signaling in CAR T cells consistently improves overall survival (Figure S1B). The survival benefit appears to be specifically mediated by IL-9, rather than by adenoviral inflammation, as the combination of CAR-IL9R T cells with Ad-GFP did not enhance survival (Figure S1B). Conversely, combining conventional CAR T cells with Ad-mIL9 resulted in a modest improvement in survival compared with Ad-mIL9 only, which may reflect low-level IL-9R expression in murine CAR T cells (Figure S1B). This notion is further supported by the weak STAT phosphorylation observed in murine CAR T cells in response to IL-9 stimulation (Figure 1C).

Given the marked antitumor efficacy observed with CAR-IL9R + Ad-mIL9 in this immunologically "cold" PDAC model, we investigated potential changes in the TME. Tumors, spleens, and blood were collected on days 5/6 post-treatment for analysis via flow cytometry and immunohistochemistry (IHC) (Figure 1K). Tumors from the CAR-IL9R + Ad-mIL9 group showed significantly higher CAR T cell infiltration, as indicated by an increase in $CD45.1^{+}$ (infused) T cells (Figure 1L). The spleens from this group also exhibited higher CAR T cell numbers compared with the group treated with conventional CAR T cells (Figure S1C), while no significant differences were observed in blood CAR T cell numbers (Figure S1D) or serum cytokine levels (Figure S1E). Since similar numbers of circulating CAR T cells were detected between cohorts, enhanced tumor infiltration observed in the CAR-IL9R + Ad-mIL9 group is likely due to improved intratumoral persistence or trafficking rather than systemic expansion. No significant differences in other immune cell populations within the TME were observed across treatment groups, as determined by flow cytometry (Figure S1F). These findings were corroborated by IHC (Figure S1G), with the exception that fewer $Ly6G^{+}$ cells were observed in the CAR-IL9R + Ad-mIL9 group, possibly indicating reduced neutrophil infiltration. Overall, IL-9-signaling CAR T cells did not substantially alter cell type composition within the TME.

(H) *In vitro* murine IL-9 (mIL-9) production by PDA7940b cells treated with Ad-mIL9, measured by ELISA. $n = 2$.
(I) Kaplan-Meier survival curves ($n = 10$ per cohort).
(J) Tumor volume progression over time. CR, complete remission.
(K) Experimental design schematic for TME analysis.
(L) Quantification of infused ($CD45.1^{+}$) T cells from tumor single-cell suspensions analyzed via flow cytometry. $n = 5$ per cohort.
Error bars indicate mean ± SEM (C, E, and F) or mean ± SD (D, H, and L). Illustrations created with Biorender.com. Statistical significance was calculated by two-way ANOVA with Bonferroni correction for multiple comparisons or Kruskal-Wallis one-way ANOVA. For Kaplan-Meier survival analysis, the log-rank Mantel-Cox test was used. Statistical significance is denoted as follows: ns, not significant; $p > 0.05$, $^{*}p \leq 0.05$, $^{**}p \leq 0.01$, $^{***}p \leq 0.001$, and $^{****}p \leq 0.0001$.
See also Figure S1.

Human IL-9-signaling CAR T cells exhibit enhanced potency and persistence in a xenograft PDAC model

To extend our findings to a human system, we next evaluated the antitumor efficacy of human IL-9 (hIL-9)-signaling CAR T cells in a xenograft flank PDAC model (Figure 2A). Immunodeficient NOD/scid/IL2rγ$^{-/-}$ (NSG) mice were implanted with the human mesothelin-expressing PDAC cell line, AsPC-1. Primary human T cells derived from healthy donors were transduced with a human mesothelin-specific CAR construct (M5 CAR) and IL-9R to enable IL-9 signaling. CAR and IL-9R transduction efficiency was assessed via flow cytometry before i.v. injection into mice. To provide an IL-9 signal to CAR-IL9R T cells, an IT injection of adenovirus encoding hIL-9 (Ad-hIL9) was administered. Prior to *in vivo* testing, IL-9 production from Ad-hIL9-transduced tumor cells was confirmed *in vitro* (Figure 2B). A dose titration study revealed that doses as low as 0.03E6 CAR-IL9R T cells combined with Ad-hIL9 were sufficient to achieve tumor clearance (Figure S2A). A higher CAR T cell dose was required in the syngeneic PDAC model, likely due to reduced murine CAR T cell potency and the presence of a functional immune system. Further survival analysis demonstrated that this low-dose combination resulted in significantly enhanced antitumor efficacy compared with CAR T cells without IL-9 signaling at a 1E6 dose (Figures 2C and 2D), underscoring the potency of IL-9-signaling CAR T cells.

To assess the *in vivo* long-term persistence of IL-9-signaling CAR T cells, we conducted a tumor rechallenge experiment. On day 90 after treatment, AsPC-1 cells were implanted into the contralateral flank of mice that had achieved complete remission of their primary tumors (Figure 2E), with treatment-naive mice serving as controls. Mice previously treated with IL-9-signaling CAR T cells rejected the newly implanted tumors and demonstrated significantly improved overall survival compared with naive controls (Figures 2F and 2G). While 2/10 mice previously treated with CAR-IL9R + Ad-hIL9 were euthanized due to signs of graft-versus-host disease (GVHD) at late timepoints, it is noteworthy that none of these mice developed tumors, highlighting the high persistence of IL-9-signaling CAR T cells.

The group receiving CAR-IL9R T cells without Ad-hIL9 also exhibited enhanced overall survival and reduced tumor progression, both in the primary tumor and upon rechallenge, as well as enhanced blood CAR T cell expansion, when compared with CAR T cells lacking IL-9R expression (Figures 2C–2G). Given that NSG mice have mast cells capable of producing mIL-9, which cross-reacts with hIL-9R,[23] and that T cells can also produce IL-9,[20] we hypothesized that either mIL-9 from NSG mice or hIL-9 from the infused CAR T cells was responsible for activating IL-9R on CAR-IL9R T cells. To test our hypothesis, we measured the levels of both mIL-9 and hIL-9 in the serum of treated mice. Our analysis revealed that hIL-9 was only detected in the group treated with Ad-hIL9 (Figure S2B, left panel), while it was undetectable in the CAR-IL9R + Ad-hIL9 group, likely due to sequestration by IL-9R-expressing CAR T cells. However, mIL-9 was detected across all treatment groups (Figure S2B, right panel). This led us to speculate that mIL-9 was responsible for activating IL-9R on CAR-IL9R T cells, contributing to the enhanced antitumor efficacy observed in the group treated with CAR-IL9R T cells alone. To test this, we treated mice with a neutralizing antibody targeting mIL-9 (α-mIL9) (Figure S2C). As expected, neutralizing mIL-9 abrogated the enhanced antitumor effects of CAR-IL9R T cells (Figures S2D and S2E). Furthermore, mice treated with CAR-IL9R T cells and α-mIL9 showed a reduced number of CAR T cells in the blood (Figure S2F). The local concentration of endogenous mIL-9 was approximately 3-fold lower than hIL-9 produced by Ad-hIL9 (Figure S2B) and therefore unlikely to impact the antitumor efficacy observed in the Ad-hIL9-treated cohorts. To further explore the potential impact of circulating IL-9 in a clinical context, we assessed hIL-9 levels in the serum of both healthy donors and patients with pancreatic cancer before and after M5 CAR T cell infusion. In our analysis, hIL-9 was undetectable in all samples (Table S1).

IL-9 signaling enhances CAR T cell expansion, persistence, and tumor infiltration *in vivo*

Flow cytometry analysis on blood samples revealed that IL-9-signaling CAR T cells expanded significantly more than conventional CAR T cells and persisted for up to 10 weeks post-treatment (Figure 3A). This expansion was associated with increased cytokine production, suggesting enhanced effector function (Figure 3B).

To assess the impact of IL-9 signaling on the phenotype of intratumoral CAR T cells, we harvested tumors from our xenograft PDAC model (Figure 3C) and performed flow cytometry analysis on single-cell suspensions of tumor samples. This analysis revealed a significantly higher infiltration of infused T cells in tumors from mice treated with IL-9-signaling CAR T cells compared with those receiving conventional CAR T cells (Figure 3D). Phenotypic analyses were not performed for the CAR-IL9R group due to low cell recovery. Tumor-infiltrating T cells from the CAR-IL9R + Ad-hIL9 group exhibited an increased proportion of early memory (CD45RA^{-}CD27^{+}) T cells compared with the CAR-only group (Figures 3E and S3A). However, when we assessed other canonical memory-associated markers such as CCR7 and CD45RO, we did not observe consistent differences between groups, suggesting that IL-9 signaling may preferentially support early memory features rather than a classical central memory phenotype (Figures S3B and S3C). Further, IL-9 signaling led to increased expansion of both CD4^{+} and CD8^{+} CAR T cells (Figure 3F); however, the relative proportions of CD4^{+} and CD8^{+} T cells remained similar between treatment groups (Figure S3D).

Tumor-infiltrating T cells from the CAR-IL9R + Ad-hIL9 group had lower expression of the co-inhibitory receptors programmed cell death protein 1 (PD-1) and T cell immunoglobulin and mucin-domain containing-3 (TIM-3) (Figures 3G and S3E). Additionally, there was a notable reduction in the percentage of double-positive PD-1^{+}TIM-3^{+} T cells, along with an increase in double-negative PD-1^{-}TIM3^{-} and PD-1^{-} lymphocyte activation gene-3 (LAG-3)$^{-}$ T cells (Figures 3H and S3E).

IL-9 signaling enhances CAR T cell function and sustains surface CAR expression, CD4^{+} T cell levels, and CD8^{+} early memory phenotype under antigen stress

To explore the mechanisms driving the enhanced antitumor efficacy of IL-9-signaling CAR T cells, we conducted *in vitro* studies on CAR-IL9R T cells. CAR and IL-9R transduction efficiency was confirmed by cell surface staining using flow

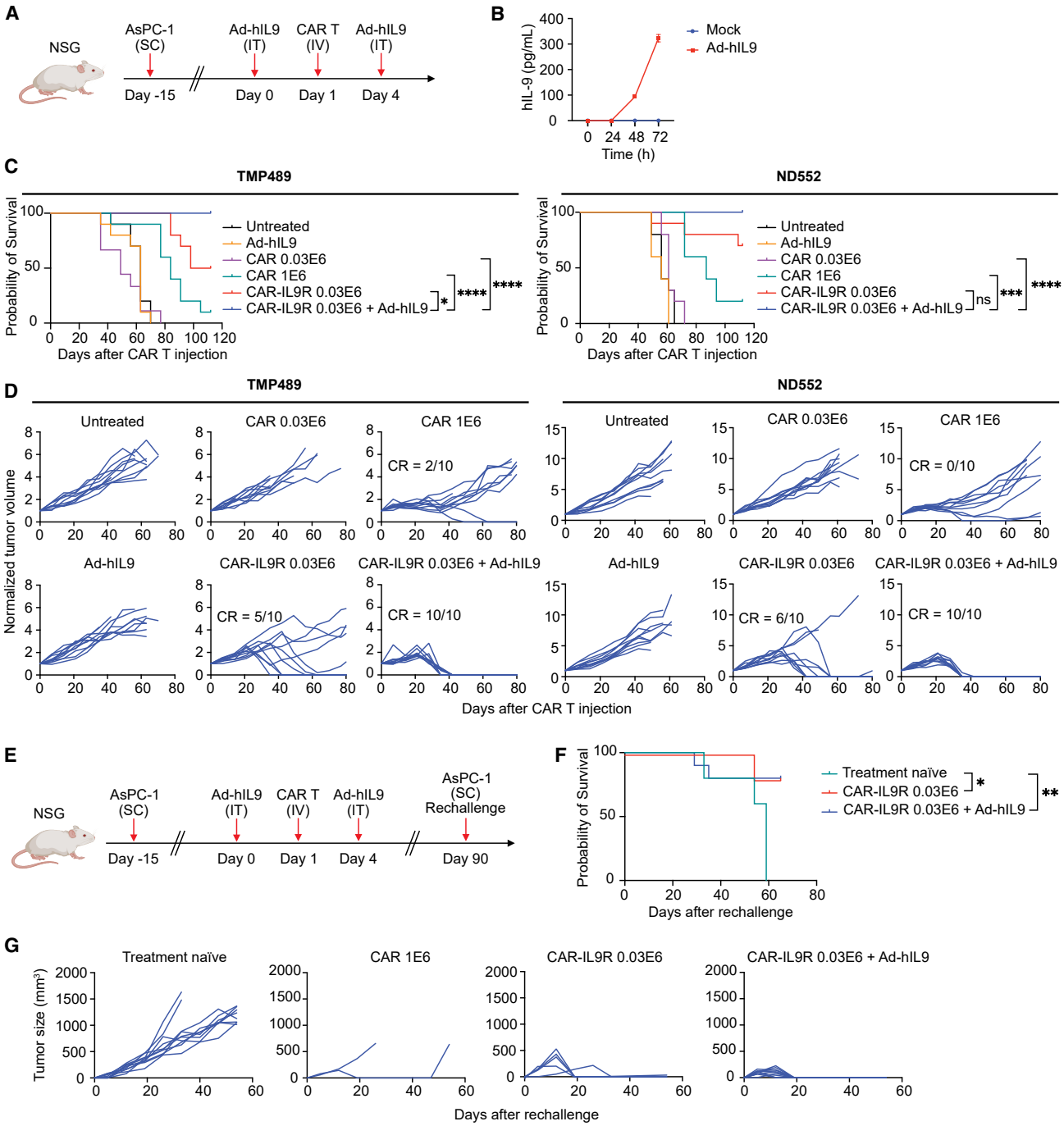

Figure 2. Human IL-9-signaling CAR T cells exhibit enhanced potency and persistence in a xenograft PDAC model

(A) Schematic of the xenograft PDAC model.

(B) *In vitro* production of human IL-9 (hIL-9) by AsPC-1 cells infected with Ad-hIL9, measured by ELISA. Error bars indicate mean ± SD (n = 3).

(C) Kaplan-Meier survival curves (n = 10 per cohort) from two independent experiments (healthy donors [HDs] = 2).

(D) Tumor volume progression over time. CR, complete remission.

(E) Schematic of tumor re-challenge study design.

(F) Kaplan-Meier survival curves for treatment-naive mice (n = 10), CAR-IL9R 0.03E6 cohort (n = 5), and CAR-IL9R + Ad-hIL9 cohort (n = 10).

(G) Tumor volume progression over time following tumor re-challenge.

Illustrations were created with Biorender.com. Statistical significance was calculated using the log-rank Mantel-Cox test. ns, not significant; $p > 0.05$, *$p \leq 0.05$, **$p \leq 0.01$, ***$p \leq 0.001$, and ****$p \leq 0.0001$.

See also Figure S2 and Table S1.

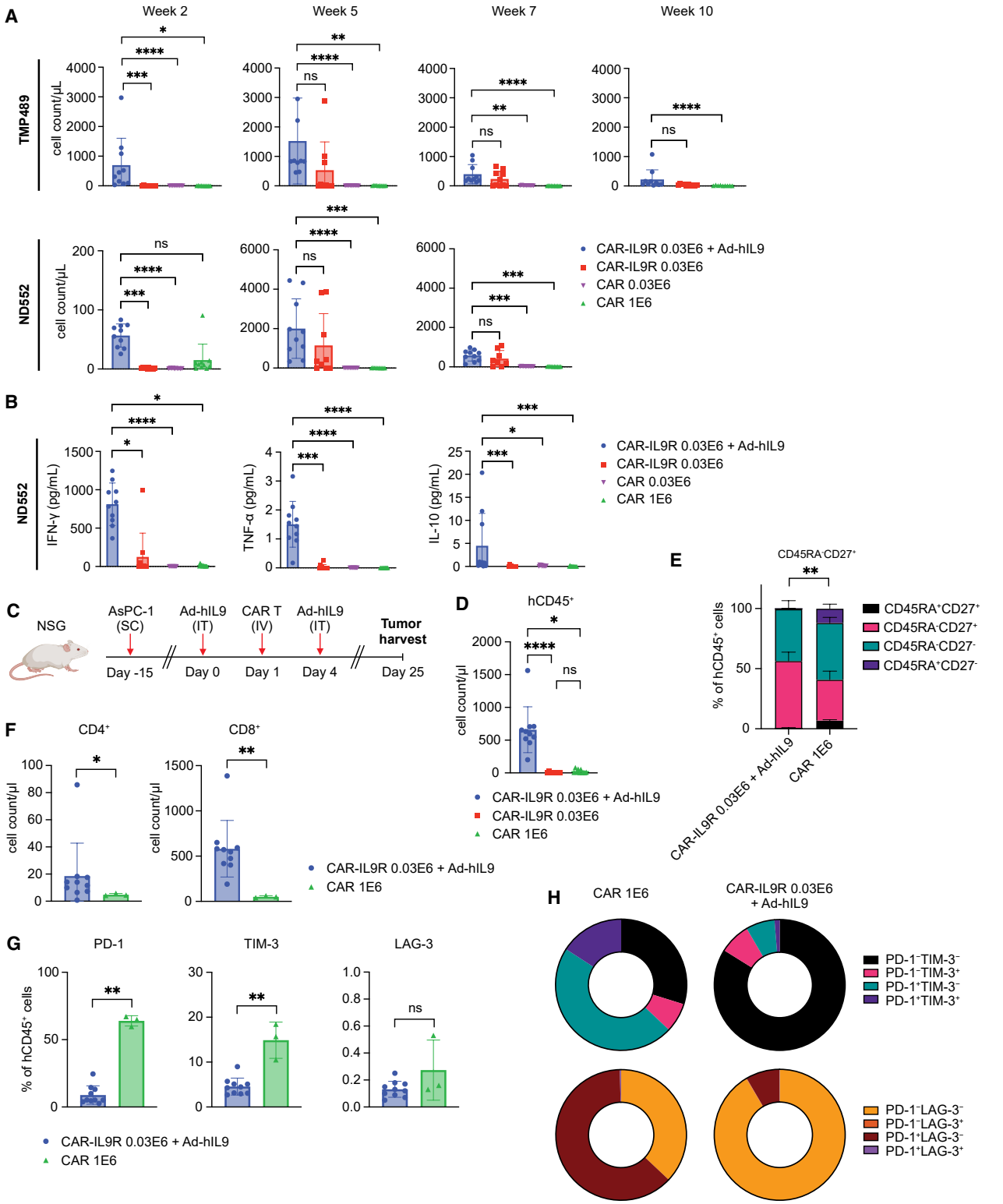

Figure 3. IL-9 signaling enhances CAR T cell expansion, persistence, and tumor infiltration *in vivo*

(A) Enumeration of infused human T cells (hCD45$^+$) in the blood analyzed via flow cytometry (n = 10 per cohort).

(B) Concentration of serum cytokines on day 22 after CAR T cell infusion (n = 10 per cohort).

(C) Schematic of the experimental design used for phenotypic analysis of tumor-infiltrating T cells following treatment. Tumors were collected on day 25 for flow cytometric analysis.

(legend continued on next page)

cytometry (Figure 4A). Consistent with results observed in mouse T cells, human CAR-IL9R T cells activated by IL-9 exhibited dose-dependent phosphorylation of STAT1, STAT3, and STAT5 (Figure 4B). We next investigated the effects of IL-9 signaling in the context of repeated antigen stimulation, using a continuous antigen exposure (CAE) assay. CAR-IL9R T cells were co-cultured with AsPC-1 cells every other day for 10 days (Figure 4C), after which they were harvested for functional assays and flow cytometry phenotyping. CAR-IL9R T cells treated with IL-9 during the CAE assay (IL-9) were compared with cells subjected to this assay in the absence of IL-9 treatment (referred to as mock-treated cells). The CAR-IL9R T cell baseline product, i.e., cells that had not undergone CAE (day 0), was used as a control. A cytotoxicity assay demonstrated that CAR-IL9R T cells undergoing stress testing in the presence of IL-9 demonstrated superior tumor cell killing compared with stress-tested mock cells, which lost cytotoxic function (Figures 4D and S4A). These enhanced cytotoxic effects were antigen-specific, as IL-9-treated cells did not eliminate tumor cells lacking mesothelin expression (Figures 4D and S4A). Consistent with the limited IL-9R expression on human CAR T cells, IL-9 treatment did not enhance tumor cell killing by CAR-only T cells (Figure S4B). Additionally, IL-9-treated cells produced higher levels of IFN-γ compared with baseline day 0 and mock cells. This increase was observed both in the absence of antigen stimulation (Figures 4E and S4C, left panel) and following co-culture with tumor cells (Figures 4E and S4C, right panel).

Flow cytometry analysis showed that, unlike mock CAR T cells, IL-9-treated CAR T cells maintained balanced $CD4^+$ and $CD8^+$ T cell proportions after repeated antigen stimulation (Figures 4F and S4D). Additionally, after stress testing, IL-9-treated CAR T cells had an increased percentage of early memory T cells ($CD45RA^-CD27^+$) compared with mock (Figures 4G and S4E). Although mock-treated CAR T cells experienced a reduction of surface CAR expression, which contributes to CAR T cell dysfunction under antigen stress,[24,25] IL-9-treated CAR T cells continued to proliferate and retained surface CAR expression (Figures 4H and S4F). The continued proliferation and maintenance of CAR expression are recognized as key mechanisms for supporting superior CAR T cell function following prolonged antigen exposure.[25]

To further dissect the mechanisms by which IL-9 signaling enhances CAR T cell function under antigen stress, we conducted single-cell RNA sequencing (scRNA-seq). CAR-IL9R T cells from three different donors were subjected to the CAE assay with or without IL-9 treatment (IL-9 and mock samples, respectively). At day 10, T cells were harvested and isolated via fluorescence-activated cell sorting (FACS) of live $EpCAM^-CD45^+$ cells, while baseline CAR-IL9R T cells were thawed and sorted for comparison (day 0 samples). A total of nine samples were sequenced using the 10× Genomics scRNA-seq platform.

Differential pseudobulk gene analysis of all CAR^+ cells revealed that the top upregulated gene in IL-9-treated CAR-IL9R T cells compared with mock-treated cells was TRERF1, a transcriptional regulatory protein known for its involvement in cholesterol metabolism and steroid hormone signaling (Figure S5A; Table S2).[26,27] Ingenuity pathway analysis (IPA) identified the Th1 pathway, IL-20 family signaling, IL-10 signaling, and cholesterol biosynthesis as some of the top pathways enriched in IL-9-treated cells (Figure S5B; Table S3). Although IL-10 has traditionally been associated with immunosuppressive roles, IL-10 can also enhance T cell antitumor immunity by modulating T cell metabolism.[28,29] Additionally, IL-10 secretion from Th1 cells is regulated by cholesterol metabolism.[30] IL-9-signaling CAR T cells exhibited elevated IL-10 secretion both *in vitro* for murine T cells (Figure 1E) and *in vivo* for human T cells (Figure 3B). This increase in IL-10 production and signaling, coupled with the upregulation of pathways involved in Th1 responses and cholesterol metabolism, prompted us to investigate the potential role of IL-10 in shaping the phenotype and function of IL-9-signaling CAR T cells.

To evaluate whether IL-10 contributes to the antitumor efficacy of IL-9-signaling CAR T cells, we employed a prostate cancer xenograft model to also confirm the antitumor effects of IL-9-signaling CAR T cells in another tumor model. We generated prostate-specific membrane antigen (PSMA)-targeted CAR (Pbbz) T cells co-expressing a dominant-negative TGF-βRII (dnTGF-βRII) and IL-9R (dnTGF-βRII-Pbbz-IL9R) (Figure S5C). A clinically tested PSMA dnTGF-βRII CAR (dnTGF-βRII-Pbbz) was used as a control.[31] NSG mice were engrafted with PC3-PSMA tumor cells and received IT Ad-hIL9 along with i.v. CAR T cell injections. Transduction efficiency was assessed via flow cytometry (Figure S5D), and IL-9 production by Ad-hIL9-transduced tumor cells was verified *in vitro* (Figure S5E). To evaluate the contribution of IL-10, an additional cohort was treated with an IL-10-neutralizing antibody (α-hIL10) (Figure S5F), and IL-10 neutralization was confirmed through serum analysis (Figure S5G). Treatment with IL-9-signaling CAR T cells at a 0.03E6 dose significantly reduced tumor progression (Figure S5H), improved overall survival (Figure S5I), and increased CAR T cell counts in the blood (Figure S5J) compared with conventional CAR T cells. IL-10 neutralization did not diminish antitumor efficacy (Figure S5H) or affect blood T cell counts (Figure S5J), indicating that IL-10 is not a major driver of the enhanced function of IL-9-signaling CAR T cells. Further, we did not observe enhanced antitumor efficacy in the CAR-IL9R-only group compared with the CAR group in the prostate cancer xenograft model, suggesting that differences in baseline mIL-9

(D) Quantification of infused $hCD45^+$ T cells within tumors, analyzed via flow cytometry (n = 10 per cohort).
(E) Flow cytometric analysis of tumor-infiltrating T cell subsets, expressed as percentages of infused $hCD45^+$ cells. Samples with fewer than 1,000 $CD45^+$ CAR T cells were excluded from flow cytometry analyses of T cell phenotypes (n = 10 for CAR-IL9R 0.03E6 + Ad-hIL9, n = 3 for CAR 1E6).
(F) Quantification of tumor-infiltrating $CD4^+$ and $CD8^+$ T cells, analyzed via flow cytometry (n = 10 for CAR-IL9R 0.03E6 + Ad-hIL9, n = 3 for CAR 1E6).
(G) Expression levels of co-inhibitory receptors PD-1, TIM-3, and LAG-3 on infused $hCD45^+$ T cells within tumors, analyzed via flow cytometry (n = 10 for CAR-IL9R 0.03E6 + Ad-hIL9, n = 3 for CAR 1E6).
(H) Pie charts illustrating the distribution of PD-1, TIM-3, and LAG-3 expression profiles among infused $hCD45^+$ T cells in the tumors, as determined by flow cytometry.
Illustration created with BioRender.com. Error bars indicate mean ± SD. Kruskal-Wallis one-way ANOVA or two-sided Mann-Whitney U tests were used for statistical analysis. ns, not significant; $p > 0.05$, $^*p \leq 0.05$, $^{**}p \leq 0.01$, $^{***}p \leq 0.001$, and $^{****}p \leq 0.0001$.
See also Figure S3.

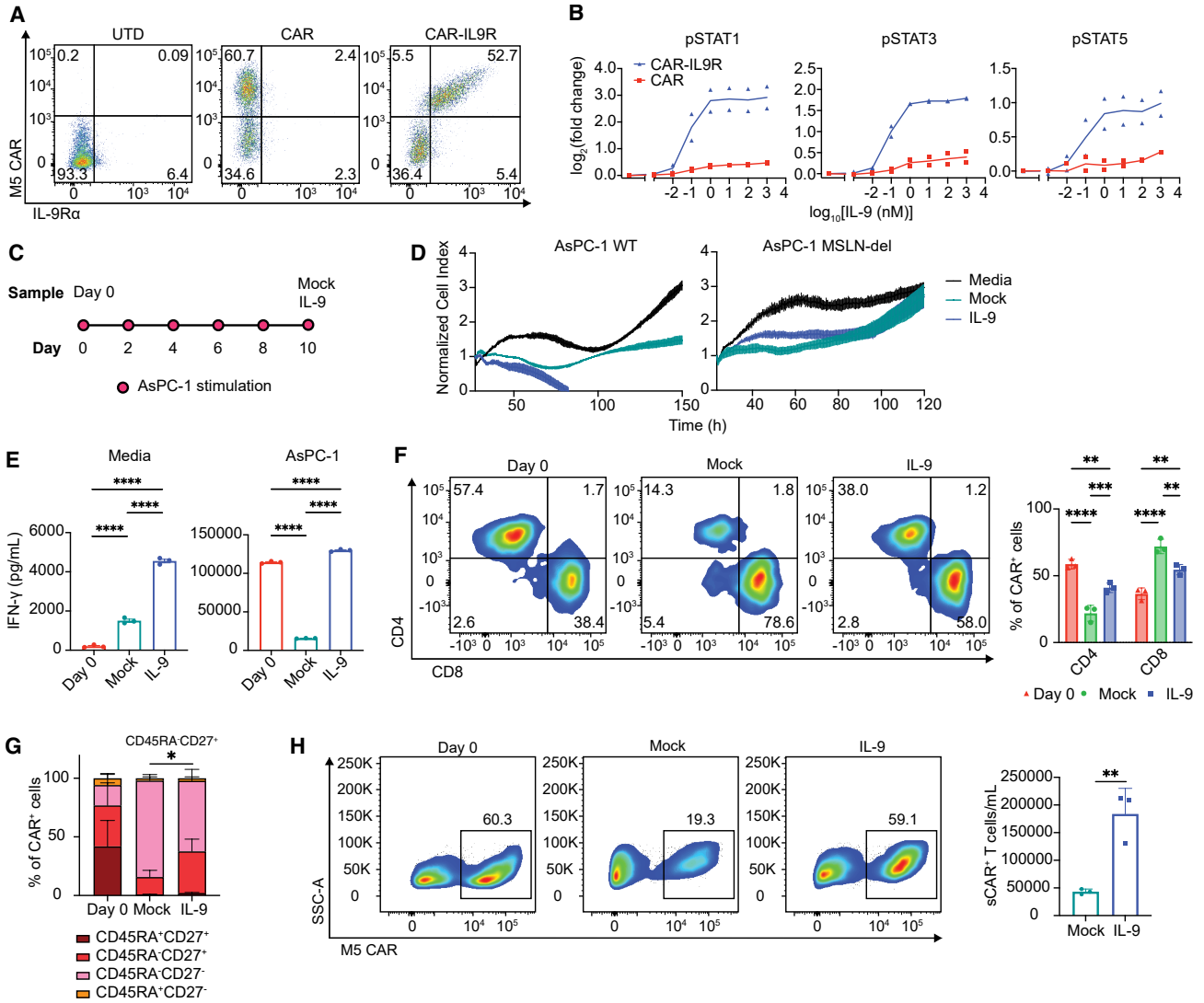

Figure 4. IL-9 signaling enhances CAR T cell function and sustains surface CAR expression, CD4⁺ T cell levels, and CD8⁺ early memory phenotype under antigen stress

(A) Flow cytometric analysis of transduction efficiency in human UTD, CAR, or CAR-IL9R T cells.

(B) Quantification of pSTAT signaling in UTD, CAR, or CAR-IL9R T cells after 20-min IL-9 stimulation. Data are shown as log fold change of mean fluorescence intensity, with mean and individual values (HD = 2).

(C) Schematic of the CAR T cell *in vitro* dysfunction model. CAR-IL9R T cells were repeatedly stimulated with AsPC-1 cells every other day for 10 days. Groups include day 0 (initial CAR-IL9R T cell product), mock (CAR-IL9R cells undergoing the CAE assay in the absence of IL-9), and IL-9 (CAR-IL9R cells undergoing the CAE assay in the presence of IL-9).

(D) *In vitro* cytotoxicity assay evaluating the lysis of mesothelin (MSLN)-positive wild-type (WT) AsPC-1 tumor cells or MSLN-deleted (MSLN-del) AsPC-1 cells by IL-9-treated or mock-treated CAR-IL9R T cells at a 1:4 E:T ratio ($n = 3$). Media was used as a control for tumor growth. Data shown are from HD ND552, and two additional donors were tested (see Figure S4A).

(E) Concentration of interferon-gamma (IFN-γ) produced by day 0, mock, or IL-9-treated CAR T cells co-cultured with media (left) or AsPC-1 cells (right) ($n = 3$). Data shown are from HD ND552, and an additional donor was tested (see Figure S4B).

(F) Left: expression of CD4 and CD8 on day 0, mock, or IL-9-treated cells. Data shown are from HD ND552, and two additional donors were tested (see Figure S4C). Right: expression of CD4 and CD8 on day 0, mock, or IL-9-treated cells, expressed as a percentage of CAR⁺ cells (HD = 3).

(G) Flow cytometric analysis of T cell subsets, expressed as percentages of CAR T cells: CD45RA⁺CD27⁺, CD45RA⁻CD27⁺, CD45RA⁻CD27⁻, or CD45RA⁺CD27⁻ ($n = 3$ donors).

(H) Left: surface CAR expression (sCAR⁺) in day 0, mock, or IL-9-treated cells. Data shown are from HD ND552, and two additional donors were tested (see Figure S4E). Right: quantification of surface CAR-expressing T cells per mL following the *in vitro* dysfunction assay (HD = 3).

Error bars indicate mean ± SD. Significance by two-way ANOVA with Tukey's post hoc test (E and F), Fisher's repeated measures Student's *t* test (G), or unpaired *t* test (H). $*p \leq 0.05$, $**p \leq 0.01$, $****p \leq 0.0001$.

See also Figures S4 and S5 and Tables S2 and S3.

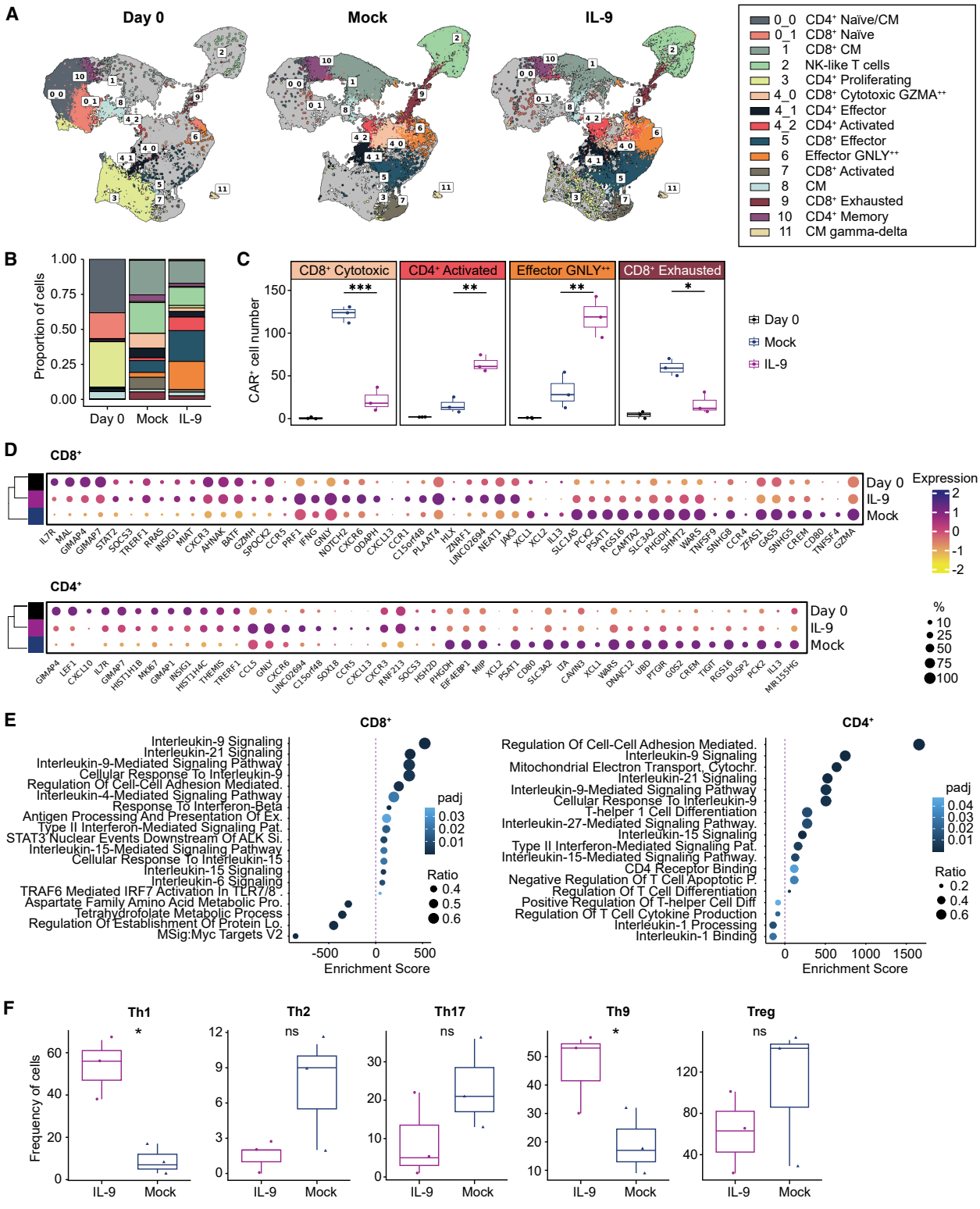

Figure 5. IL-9 treatment enhances CAR T cell effector phenotype and reduces dysfunction under antigen stress

(A) Uniform manifold and approximation projection (UMAP) visualization of scRNA-seq data from day 0 (day 0) T cells as well as IL-9-treated and mock-treated T cells harvested after the CAE assay (HD = 3). UMAP clusters are color-coded, with annotations shown in the right panel.

(B) Bar graph illustrating the proportion of day 0, IL-9-treated, and mock-treated T cells by cluster. Data were down sampled uniformly across treatments and clusters to ensure comparability.

(legend continued on next page)

levels between the PDAC and prostate models may influence the outcome.

IL-9 treatment enhances CAR T cell effector phenotype and reduces dysfunction under antigen stress

To further investigate how IL-9 signaling contributes to the improved antitumor activity of CAR T cells, we conducted detailed analysis of scRNA-seq data. Semi-unsupervised clustering using uniform manifold approximation and projection (UMAP) identified 15 distinct T cell clusters (Figures 5A and S6).[32] Analysis of cluster distribution revealed a higher proportion of cells in effector clusters within the IL-9-signaling group (Figure 5B). Specifically, CAR$^+$ T cells in the IL-9-treated group showed a significant increase in the CD4$^+$ activated and *GNLY*$^{++}$ effector clusters. By contrast, the mock group exhibited higher proportions of CAR$^+$ cells in CD8$^+$ exhausted and *GZMA*$^{++}$ cytotoxic clusters (Figure 5C). The day 0 samples displayed typical distributions of naive and effector cells, as expected from cells that had not yet encountered antigen (Figures 5B and 5C).

Next, we investigated differential gene expression in the CD8$^+$ and CD4$^+$ CAR$^+$ compartments (Figure 5D; Table S4).[33] IL-9 treatment in CD8$^+$ T cells led to higher expression of transcription factors (TFs) such as *TRERF1*, *BATF*, *STAT2*, and *HLX*, along with increased expression of chemokine-related genes like *CXCL13*, *CCR1*, *CCR5*, *CXCR6*, and *CXCR3*. Markers of naive or memory CD8$^+$ T cells, such as *IL7R*, and cytotoxicity-related genes like *GNLY*, *IFNG*, *GZMH*, and *PRF1* were also increased. By contrast, expression of genes linked to activation, including *GZMA*, *TNFSF4* (OX-40L), *CD80*, and *TNFSF9* (4-1BBL), was reduced. Since sustained expression of T cell activation genes is often linked to exhaustion states,[34] their reduction in IL-9-treated cells may indicate decreased dysfunction. In CD4$^+$ T cells, IL-9 treatment similarly increased expression of chemokine-related genes, including *CXCL10*, *CCL5*, *CXCR6*, *CCR5*, *CXCL13*, and *CXCR3*, along with markers of naive/memory T cells (*LEF1* and *IL7R*). Additionally, there was increased expression of proliferation-associated genes such as *MKI67* and cytotoxicity-related genes like *GNLY*, while *CD80* and *TIGIT* were decreased. Unsupervised hierarchical clustering revealed that IL-9-treated CAR$^+$ cells retained a transcriptional profile more closely aligned with day 0 samples than the mock group for both CD8$^+$ and CD4$^+$ CAR$^+$ cells (Figure 5D), suggesting that IL-9 treatment promotes less differentiated T cell states compared with mock.

Gene set enrichment analysis (GSEA)[35] revealed significant enrichment of interleukin signaling pathways in IL-9-treated CD8$^+$ CAR$^+$ T cells, including IL-4, IL-6, IL-15, IL-21, and type II interferon responses. A similar pattern was observed in CD4$^+$ CAR$^+$ cells, where IL-21, IL-27, IL-15, and type II interferon signaling pathways were significantly enriched, along with those promoting Th1 differentiation and cell-cell adhesion (Figure 5E; Table S5). Signature scoring confirmed an elevated frequency of Th1 cells and Th9 cells in the IL-9-treated group, with no notable changes in Th2, Th17, or Treg populations (Figure 5F).

IL-9 signaling directs CAR$^+$ CD8$^+$ T cells toward central memory clusters and away from dysfunctional clusters under antigen stress

We investigated the impact of IL-9 on CAR T cell differentiation by analyzing CAR$^+$ cell trajectories along pseudotimes using a semi-unsupervised approach.[36] We identified six distinct trajectories: three for CD8$^+$ cells, two for CD4$^+$ cells, and one combined CD8$^+$/CD4$^+$ (Figures 6 and S7A), with four trajectories showing significant differences between IL-9-treated and mock conditions (Figure 6A).

In the first CD8$^+$ trajectory, cells progressed from naive to central memory populations (Figure 6A and 6B). IL-9 treatment increased the number of CAR$^+$ cells along this path, without altering the distribution of cell weights along the trajectory. These data align with the observed increase in the proportion of tumor-infiltrating early memory T cells in mice from the xenograft PDAC model treated with IL-9 signaling compared with conventional CAR T cells (Figure 3E). Differential expression analysis identified genes statistically different along the trajectory with the addition of IL-9, including genes involved in migration (*TIAM1*) that increased over pseudotime compared with mock (Figures 6B and S7B).[37] In the second CD8$^+$ trajectory, cells progressed from a naive state through cytotoxic stages, culminating in T cells with robust effector function (Figures 6A and 6C). IL-9 treatment influenced cell distribution along the pseudotime, resulting in more IL-9-signaling CAR T cells reaching a strong effector state, consistent with the increased proportion of cells in the Effector *GNLY*$^{++}$ cluster (Figure 5C). In this trajectory, IL-9 treatment led to increased expression of cytotoxicity-related genes (*GNLY* and *GZMB*), whereas low expression of genes involved in T cell differentiation (*SOS1*) and regulation of T cell responses (*TNFSF13B*) was maintained along the pseudotime (Figures 6C and S7B). The third CD8$^+$ trajectory showed cells progressing from naive through cytotoxic states to exhausted and dysfunctional states resembling natural killer (NK)-like cells (Figures 6A and 6D). This progression, consistent with findings in our solid tumor model of CAR T cell dysfunction, occurs when CAE drives CD8$^+$ T cells to transition into NK-like

(C) Boxplots displaying the number of CAR$^+$ cells per cluster for day 0, IL-9-treated, and mock-treated groups. Data are based on downsampled samples (to the lowest CAR$^+$ cell count across donors), and values reflect absolute cell counts. Only clusters showing statistically significant differences in CAR$^+$ cell numbers between IL-9-treated and mock-treated groups are shown.

(D) Dot plot illustrating differentially expressed (DE) genes between day 0, IL9-treated, and mock-treated groups within CD4$^+$ and CD8$^+$ CAR$^+$ T cells with adjusted p values < 0.05. Dot size represents the percentage of cells expressing each gene, while color intensity denotes expression levels.

(E) GSEA of CD4$^+$ and CD8$^+$ CAR$^+$ cells. Dot size reflects the ratio of genes in each pathway, and color intensity denotes statistical significance (padj, adjusted p value).

(F) Frequency distribution of IL9-treated and mock-treated CD4$^+$ CAR$^+$ subsets, assessed by signature scoring.

Cluster composition analysis was performed using Welch's t test. DE statistical analysis was performed using Motif Alignment and Search Tool (MAST). Signature scores were calculated as the area under the curve. Donor comparisons between treatment groups were conducted using Fisher's repeated measures Student's t test. ns, not significant; $p > 0.05$, $^*p \leq 0.05$, $^{**}p \leq 0.01$, $^{***}p \leq 0.001$, and $^{****}p \leq 0.0001$.

See also Figure S6 and Tables S4 and S5.

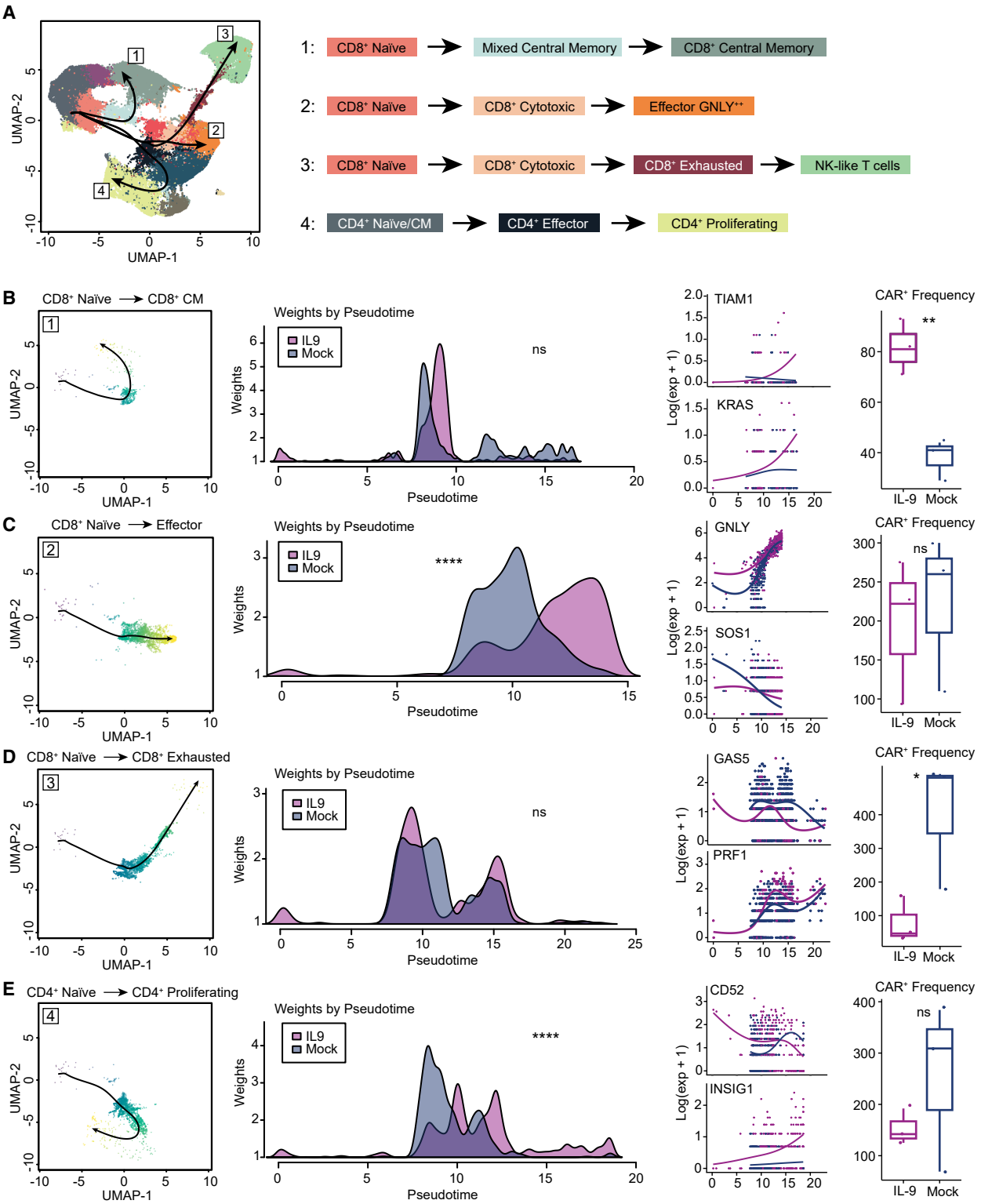

Figure 6. IL-9 signaling directs CAR⁺ CD8⁺ T cells toward CM clusters and away from dysfunctional clusters under antigen stress

(A) UMAP visualization of four identified trajectories overlayed on clusters, with corresponding cluster paths diagramed on the right.

(B) CD8⁺ naive to CD8⁺ central memory (CM) trajectory. Left, UMAP; middle, weights by pseudotime; right, differential expression of select genes along the trajectory and CAR⁺ cell distribution frequency along the trajectory.

(C) CD8⁺ naive to CD8⁺ Effector GNLY⁺⁺ trajectory. Left, UMAP; middle, weights by pseudotime; right, differential expression of select genes along the trajectory and CAR⁺ cell distribution frequency along the trajectory.

(legend continued on next page)

states.[24] Fewer cells followed this path in the IL-9-treated group, suggesting that IL-9 may redirect CAR T cell progression away from an exhausted state. This aligns with the reduced proportion of IL-9-signaling T cells observed in the CD8$^+$ exhausted cluster (Figure 5C). Multiple genes differ by treatment, including *GAS5*, *PRF1*, and chemokine/cytokine-related genes (*CCL5*, *IL13*, and *CCL1*) (Figures 6D and S7B).

The CD4$^+$ trajectory, trajectory 4, transitioned from naive to effector and ultimately to proliferating states (Figures 6A and 6E). IL-9 treatment promoted this cycling, as more cells reached the trajectory's terminal point. Conversely, mock-treated CAR$^+$ cells stalled in effector states. This suggests that IL-9 actively supports a return to proliferative states in CD4$^+$ CAR T cells. Although the proliferating cluster (cluster 3) contained both CD4$^+$ and CD8$^+$ T cells, it was predominantly composed of CD4$^+$ cells (75.5%), supporting the relevance of this trajectory to CD4$^+$ cell dynamics. Differentially expressed genes along this trajectory included decreased expression of *CD52*, involved in regulating T cell responses, and increased expression of the cholesterol biosynthesis gene *INSIG1* and proliferation marker *MKI67* (Figures 6E and S7B).

Together, these findings indicate that IL-9 signaling influences CAR T cell differentiation under antigen stress, enhancing CD8$^+$ CAR T cell progression toward central memory and effector states, and promoting proliferation in CD4$^+$ cells.

RNA velocity and TF analyses provide mechanistic insights into how IL-9 signaling redirects CAR T cell fate

To independently validate our trajectory findings, we performed RNA velocity analysis to study changes in gene expression over time. RNA velocity defines vectors that predict the future state of individual cells based on the ratio of spliced and unspliced mRNA, with the assumption that more differentiated cells have a higher proportion of spliced mRNA.[38] We found that spliced mRNA progressively increased from day 0 (40%) to IL-9-treated (42%) and mock-treated cells (44%), indicating a higher proportion of differentiated cells in the mock-treated group (Figure 7A).

Further RNA velocity analyses revealed that IL-9 signaling significantly altered the rate and direction of change of CAR T cells exposed to antigen stress over time. In mock-treated CAR T cells, velocity vectors predominantly followed a path from the top left to the bottom right of the UMAP plot (Figure 7B). By contrast, in IL-9-treated CAR T cells, velocity vectors also showed a distinct horizontal progression, marked by violet-colored vectors, indicating movement away from terminal states and toward less differentiated fates. This horizontal directional progression includes vectors laterally exiting the Exhaustion cluster and vectors progressing from an Effector *GNLY*$^{++}$ cluster toward a predicted future CD4$^+$ proliferating state. Overall, RNA velocity predicts that IL-9 signaling drives CAR T cells toward less differentiated and more proliferative effector states under antigen stress compared with conventional CAR T cells (Figure 7B).

Both trajectory and RNA velocity analyses indicate that IL-9 signaling promotes the transition of CAR T cells toward functional rather than dysfunctional states. This transition fosters the development of proliferative and effector T cells under antigen stress. Despite relying on distinct inputs, the results from these two methods are consistent: RNA velocity employs the relative abundance of spliced versus unspliced mRNA to infer the rate and direction of cell-state transitions, whereas trajectory analysis relies on a count matrix and minimum spanning tree (MST) modeling. Together, these complementary approaches validate our conclusion that IL-9 signaling promotes CAR T cell memory and proliferation over terminal differentiation, promoting the dramatically enhanced potency of CAR-IL9R T cells.

To further investigate the transcriptional mechanisms underlying the phenotypic differences between IL-9-treated and mock-treated CAR T cells, we analyzed regulatory interactions between TFs and target genes from our scRNA-seq data using the Transcriptional Regulatory Relationships Unraveled by Sentence-based Text-mining (TRRUST) human database (Table S6).[39] Results were confirmed using IPA upstream regulatory analysis (Table S7). These analyses identified transcriptional regulatory networks that may explain the differences observed in mock-treated and IL-9-treated CAR-IL9R T cells under antigen stress (Figure 7C). IL-9 treatment strongly enriched STAT4 activity in both CD4$^+$ and CD8$^+$ CAR T cells (Figures 7C and S7C). This was unexpected because STAT4 has not previously been associated with IL-9 signaling. Additionally, STAT4 activity was elevated in IL-9-treated and baseline CAR T cells compared with mock, specifically within cluster 9 (CD8$^+$ exhausted) (Figures S7C and S7D). Both STAT1 and STAT3 are established mediators of γ_c cytokine signaling, including IL-9, while STAT4 traditionally supports Th1 responses via IL-12 signaling. IL-9 treatment also enriched STAT1 activity, known to mediate IFN-γ functions.[40] The upstream transcription factor 1 (USF1) TF pathway was also elevated in both CD8$^+$ and CD4$^+$ CAR T cells; however, the STAT3 pathway was only induced in CD8$^+$ CAR T cells. STAT3 signaling has been shown to drive T cell memory formation.[41] Additionally, the USF1 TF, which regulates genes involved in sugar and lipid metabolism[42,43] may provide a proliferative advantage to IL-9-signaling CAR T cells.

Both CD8$^+$ and CD4$^+$ IL-9-signaling CAR T cells exhibit downregulation of TF pathways associated with T cell activation such as v-rel avian reticuloendotheliosis viral oncogene homolog A (RELA) and nuclear factor kappa B subunit 1 (NFkB1) under antigen stress, potentially reducing T cell dysfunction. Further, IL-9-signaling CD8$^+$ CAR T cells exhibit decreased levels of activating transcription factor 4 (ATF4), hypoxia-inducible factor 1

(D) CD8$^+$ naive to CD8$^+$ exhausted trajectory. Left, UMAP; middle, weights by pseudotime; right, differential expression of select genes along the trajectory and CAR$^+$ cell distribution frequency along the trajectory.
(E) CD4$^+$ naive to CD4$^+$ proliferating trajectory. Left, UMAP; middle, weights by pseudotime; right, differential expression of select genes along the trajectory and CAR$^+$ cell distribution frequency along the trajectory.
Weighted pseudotime comparisons were performed by the Wilcoxon rank-sum test with continuity correction. Differential gene expression along trajectories was calculated using a negative binomial generalized additive model (NB-GAM). Comparisons of CAR$^+$ cell frequencies between treatments were conducted by Fisher's repeated measures Student's *t* test. ns, not significant; $p > 0.05$, $^*p \leq 0.05$, $^{**}p \leq 0.01$, $^{***}p \leq 0.001$, and $^{****}p \leq 0.0001$.
See also Figure S7.

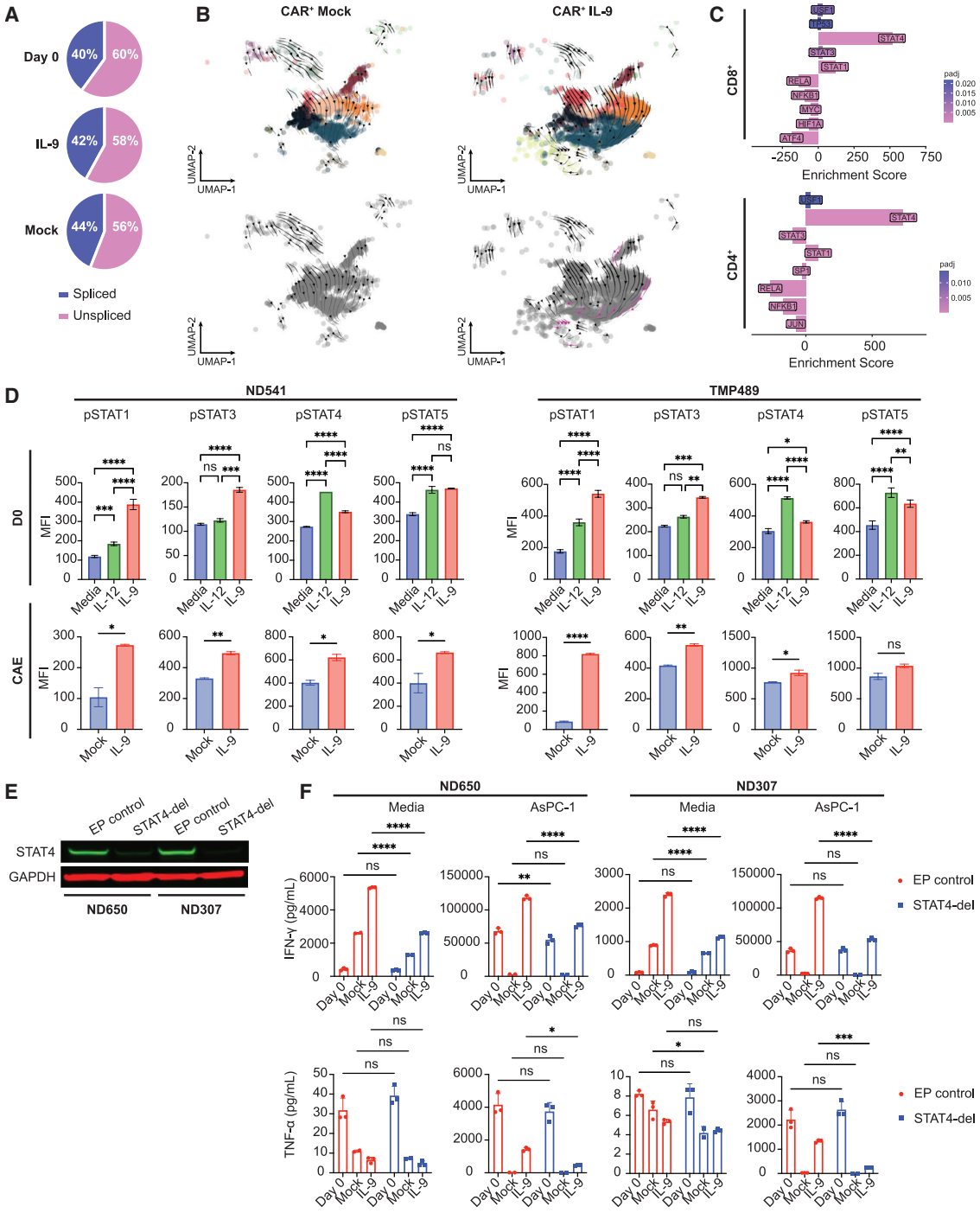

Figure 7. RNA velocity and TF analyses provide mechanistic insights into how IL-9 signaling redirects CAR T cell fate

(A) Pie charts illustrating the fractions of spliced and unspliced reads in T cells for day 0, IL-9-treated, and mock-treated groups.

(B) Velocity fields projected onto UMAPs for IL-9-treated and mock-treated CAR$^+$ cells. The top panels display UMAPs colored by clusters, while the bottom panels show black-and-white UMAPs to enhance the visualization of velocity vectors. Violet arrows indicate vectors predicting future states that shift from right to left and/or upward.

(C) TF enrichment analysis of IL-9-treated versus mock-treated CAR-IL9R T cells under antigen stress. Differentially expressed genes with a log fold change greater than ±1 were analyzed using the TRRUST database, with results filtered to include only those with an adjusted *p* value (padj) ≤ 0.02.

(D) Top: quantification of pSTAT signaling in CAR-IL9R T cells after 20-min stimulation with IL-9, IL-12, or media as a control. Data are shown as mean fluorescence intensity (MFI). Bottom, quantification of pSTAT signaling in CAR-IL9R T cells after the *in vitro* dysfunction assay either in the absence (mock) or presence of IL-9 treatment. HD = 2.

(legend continued on next page)

alpha (HIF-1α), and MYC pathways, suggesting a lower cellular stress response. These results provide mechanistic insight into how IL-9 signaling reprograms CAR T cell differentiation upon repeated antigen exposure, enhancing central memory formation and reducing exhaustion in $CD8^+$ T cells while fostering a proliferative effector phenotype in $CD4^+$ T cells to potentiate antitumor efficacy, CAR T cell expansion, and persistence *in vivo*.

Given the surprising enrichment of STAT4 transcriptional activity in our scRNA-seq dataset, we next sought to validate this at the protein level. Upon IL-9 stimulation of day 0 CAR-IL9R T cells, we observed robust phosphorylation of STAT4, alongside expected activation of STAT1, STAT3, and STAT5 (Figure 7D, top). IL-12 stimulation served as a positive control for STAT4 activation. To assess whether this activation was maintained under antigen stress, we analyzed CAR T cells following the CAE assay and found that IL-9-treated samples exhibited higher levels of phosphorylated STAT4 compared with mock-treated controls (Figure 7D, bottom).

To investigate whether STAT4 contributes to the phenotype and function of IL-9-signaling CAR T cells under antigen stress, we performed CRISPR-Cas9-mediated STAT4 deletion (STAT4-del) in human T cells, followed by transduction with the CAR-IL9R construct and expansion. After confirming the deletion was successful (Figure 7E), we subjected these cells to the CAE assay, exposing them to repeated antigen stimulation either in the absence (mock) or presence of IL-9. As a control, we used T cells electroporated under identical conditions but without guide RNAs (EP control). STAT4-del significantly reduced IFN-γ production in IL-9-treated CAR T cells compared with the EP control, consistent with IFN-γ being a known downstream target of STAT4 signaling (Figure 7F). STAT4-del cells also displayed reduced production of TNF-α, another cytokine associated with Th1 responses (Figure 7F). In addition to the decrease in cytokine production, STAT4-del cells exhibited a modest increase in memory markers and a minimal reduction in *in vitro* cytotoxicity (Figure S7E). These results demonstrate that STAT4 contributes to IL-9-mediated effector function, predominantly through IFN-γ production.

In summary, IL-9 signaling redirects $CD4^+$ and $CD8^+$ CAR T cell fate, primarily through STAT1 and STAT4 signaling, to enable less differentiated and exhaustion-resistant states, enhancing their efficacy against solid tumors.

DISCUSSION

A major obstacle hindering the effectiveness of CAR T cell therapies targeting solid tumors, which comprise over 90% of diagnosed cancers,[44] is limited CAR T cell infiltration into the TME, and CAR T cells that do penetrate the tumor often become dysfunctional.[45] This study addresses these critical barriers by endowing CAR T cells with ectopic IL-9 signaling to enhance antitumor efficacy. Our findings show that IL-9 signaling directs $CD8^+$ CAR T cells toward less differentiated T cell fates, enriching memory-like features strongly associated with long-term remission in CAR T cell patients[46,47] and reducing CAR T cell dysfunction negatively correlated with clinical efficacy.[48] Consistent with this, we observed that IL-9-signaling CAR T cells had potent effects in our xenograft PDAC and prostate tumor models even at low CAR T cell doses. The CAR T cells persisted in circulation for up to 10 weeks, and tumor rechallenge led to rapid tumor rejection, underscoring the potential of IL-9 signaling to enhance CAR T cell function and persistence.

Additionally, trajectory and RNA velocity analyses indicate that IL-9-treated CAR T cells progress toward less differentiated, proliferative $CD4^+$ clusters, suggesting enhanced proliferative potential in response to IL-9 signaling. We observed that IL-9 signaling promotes $CD4^+$ CAR T cell differentiation toward Th1 cells, a process accompanied by increased secretion of IFN-γ and TNF-α, both critical for antitumor responses. The TF STAT4 is essential for Th1 differentiation and the production of pro-inflammatory cytokines, and STAT4-deficient mice exhibit a profound Th1 defect.[49,50] Our data suggest that in IL-9-signaling CAR T cells, IL-9, rather than IL-12, promotes Th1 differentiation through induction of the STAT4 pathway and enhanced IFN-γ and TNF-α secretion. These findings align with a previous study in acute myeloid leukemia, where IL-9 secretion by leukemia stem cells induces Th1 polarization.[51] Th1 cells and their cytokines are strongly associated with better clinical outcomes across multiple cancer types,[52] and Th1 differentiation is linked to improved efficacy in adoptive cell therapies.[53,54] In addition, IL-9-signaling CAR T cells also retain a population of Th2-polarized CAR T cells. Elevated Th2 functionality in CAR T infusion products correlates with long-term CAR T cell persistence and superior outcomes in pediatric hematologic malignancies.[55] In our study, IL-9 treatment also increases the percentage of Th9 cells, which have been implicated in antitumor responses in preclinical solid tumor models.[14,15] Collectively, $CD4^+$ IL-9-signaling CAR T cells, polarized toward Th1 and Th9 cells while maintaining Th2 cells, exhibit superior antitumor efficacy and persistence both *in vitro* and *in vivo*.

STAT4-deficient cells also exhibited a subtle increase in the frequency of early memory cells in STAT4-deficient CAR T cells. This may reflect compensatory enrichment of STAT3 activity, which has been linked to memory T cell formation. Similar competitive dynamics among STAT family members have been described, where loss of one STAT can lead to increased activity of others.[56] For example, the STAT3 regulon is enriched in IL-9R-expressing T cells lacking STAT1 signaling, supporting the idea that cross-regulation among STATs influences transcriptional

(E) Representative western blot showing STAT4 protein expression in electroporated (EP) control and STAT4-deleted (STAT4-del) CAR-IL9R T cells. GAPDH was used as a loading control.

(F) Concentration of interferon-gamma (IFN-γ) produced by EP control and STAT4-deleted (STAT4-del) CAR-IL9R T cells. Day 0, mock, or IL-9-treated CAR-IL9R T cells after undergoing the *in vitro* dysfunction assay were co-cultured with media or AsPC-1 cells, and IFN-γ concentration was determined by cytometric bead array ($n = 3$). HD = 2.

Error bars indicate mean ± SD. Statistical significance was determined using a two-way ANOVA followed by Tukey's (D) or Sidak's (F) post hoc test. ns, not significant; $p > 0.05$, $^*p \leq 0.05$, $^{**}p \leq 0.01$, $^{***}p \leq 0.001$, and $^{****}p \leq 0.0001$.

See also Figure S7 and Tables S6 and S7.

outcomes (Jiang et al.[18]). This may represent a similar "Goldilocks" phenomenon for STAT4, where complete ablation shifts the balance between effector and memory differentiation.

In summary, we engineered CAR T cells to incorporate IL-9 signaling and assessed the impact on antitumor efficacy and phenotypic characteristics. Even at low doses, IL-9 signaling significantly enhanced CAR T cell expansion, persistence, and tumor infiltration, leading to improved tumor clearance and prolonged survival in *in vivo* models of pancreatic and prostate cancer. Under antigen stress, IL-9 fosters a favorable phenotype, characterized by enhanced memory formation, reduced expression of ATF4, and reduced dysfunction in $CD8^+$ CAR T cells. Coupled with increased effector proliferation in $CD4^+$ CAR T cells, this yields less differentiated and more potent CAR T cells. These findings position IL-9 signaling as a promising strategy to overcome key barriers in CAR and T cell receptor (TCR) T cell therapies targeting solid tumors.

Limitations of the study

Although STAT4 deletion revealed functional effects on cytokine production, compensatory activation of other STAT family members, such as STAT1 or STAT3, may have masked the full extent of STAT4-dependent effects. Further work is necessary to understand the contribution of the activation of individual STAT members to the enhanced phenotype observed for IL-9 signaling CAR T cells. Additionally, even though we did not observe major effects of IL-9 signaling on the TME, spatial organization and human-specific features of the TME were not assessed and may contribute to IL-9-mediated activity.

RESOURCE AVAILABILITY

Lead contact

Requests for further information, resources, and reagents should be directed to and will be fulfilled by the lead contact, Dr. Carl H. June (cjune@upenn.edu).

Materials availability

CAR constructs will be available under a material transfer agreement upon request. The sgRNAs and primer sequences are listed in the key resources table.

Data and code availability

- ScRNA-seq data generated in this study are available through GEO. The accession number is listed in the deposited data section of the key resources table.
- This paper does not report original code. Programs used to analyze scRNA-seq data are listed in the STAR Methods.

ACKNOWLEDGMENTS

We would like to thank Donna Gonzales, Tong Da, Carolyn Shaw, Yujie Ma, John Scholler, Ting-Jia Fan, Andrew Rech, John Tobias, and Enrico Radaelli for technical assistance and/or helpful discussions. We also thank the Translational and Correlative Studies Laboratory (TCSL) at the University of Pennsylvania (UPENN) for their generous provision of patient serum samples, the Human Immunology Core (HIC) at UPENN, the Genomics Facility at the Wistar Institute, and the Comparative Pathology Core (CPC) at the School of Veterinary Medicine. Funding was provided by the Mark Foundation (19-011MIA), Prostate Cancer Foundation (PCF) TACTICAL grant (22-TACT03), the Parker Institute for Cancer Immunotherapy (PICI) (C-04339), the UPENN Vet Comparative Pathology Core Facility (RRID: SCR_022438), the Abramson Cancer Center Support Grant (P30 CA016520), and the NIH Shared Instrumentation Grant (S10 OD023465-01A1). S.C. is supported by the PICI Rise Scholar Award. U.U. is supported by a Mildred-Scheel-Postdoctoral Fellowship of the German Cancer Aid.

AUTHOR CONTRIBUTIONS

Conceptualization, S.C., R.M.Y., and C.H.J.; methodology, S.C., R.M.Y., W.V.W., P.C.R., and M.A.A.; investigation, S.C., U.U., A.V.F., C.-A.A., S.J.A., and M.S.; formal analysis, S.C. and W.V.W.; visualization, S.C. and W.V.W.; funding acquisition, S.C., R.M.Y., and C.H.J.; project administration, S.C. and R.M.Y.; supervision, R.M.Y. and C.H.J.; writing – original draft, S.C.; writing – review & editing, S.C., R.M.Y., and C.H.J.; writing – editing, W.V.W., U.U., A.V.F., C.-A.A., S.J.A., and M.S.

DECLARATION OF INTERESTS

R.M.Y., S.C., M.A.A., and P.C.R. are inventors on patent(s) and/or patent application(s) licensed to Kite Pharma and/or Novartis Institutes of Biomedical Research and receive license revenue from such licenses. C.H.J. is an inventor on patents and/or patent applications licensed to Novartis Institutes of Biomedical Research, Kite Pharma, Capstan Therapeutics, Dispatch Biotherapeutics, and BlueWhale Bio. C.H.J. is a member of the scientific advisory boards of AC Immune, BluesphereBio, BlueWhale Bio, Cabaletta, Carisma, Cartography, Cellares, Celldex, Decheng, Poseida, Replay Bio, Verismo, and WIRB-Copernicus. M.S. is an inventor on patents and/or patent applications licensed to Kite Pharma and Dispatch Biotherapeutics.

STAR★METHODS

Detailed methods are provided in the online version of this paper and include the following:

- KEY RESOURCES TABLE
- EXPERIMENTAL MODEL AND STUDY PARTICIPANT DETAILS
  - Cell lines
  - Mice
  - Human Samples
- METHOD DETAILS
  - General cell culture
  - Murine CAR T cell production
  - Human CAR T cell production
  - Phosphoflow signaling assay
  - CAR T cell *in vitro* dysfunction model
  - Cytokine production assays
  - *In vitro* cytotoxicity assays
  - Xenograft animal models
  - Syngeneic animal model
  - Caliper measurements of subcutaneous tumors
  - Processing of tumors and spleens
  - Peripheral blood (CAR) T cell analysis
  - Cytokine analysis from mouse serum
  - Immunohistochemistry (IHC)
  - Flow cytometry and sorting
  - Single-cell RNA sequencing (scRNA-seq)
  - scRNA-seq data quality control
  - scRNA-seq data analysis
  - CRISPR/Cas9-Mediated STAT4 deletion
  - Validation of STAT4 deletion
- QUANTIFICATION AND STATISTICAL ANALYSIS

SUPPLEMENTAL INFORMATION

Supplemental information can be found online at https://doi.org/10.1016/j.immuni.2025.10.021.

Received: January 17, 2025
Revised: August 7, 2025
Accepted: October 27, 2025
Published: November 21, 2025

REFERENCES

1. June, C.H., and Sadelain, M. (2018). Chimeric Antigen Receptor Therapy. N. Engl. J. Med. *379*, 64–73. https://doi.org/10.1056/NEJMra1706169.
2. Melenhorst, J.J., Chen, G.M., Wang, M., Porter, D.L., Chen, C., Collins, M.A., Gao, P., Bandyopadhyay, S., Sun, H., Zhao, Z., et al. (2022). Decade-long leukaemia remissions with persistence of CD4(+) CAR T cells. Nature *602*, 503–509. https://doi.org/10.1038/s41586-021-04390-6.
3. Sterner, R.C., and Sterner, R.M. (2021). CAR-T cell therapy: current limitations and potential strategies. Blood Cancer J. *11*, 69. https://doi.org/10.1038/s41408-021-00459-7.
4. Bell, M., and Gottschalk, S. (2021). Engineered Cytokine Signaling to Improve CAR T Cell Effector Function. Front. Immunol. *12*, 684642. https://doi.org/10.3389/fimmu.2021.684642.
5. Atkins, M.B., Sparano, J., Fisher, R.I., Weiss, G.R., Margolin, K.A., Fink, K.I., Rubinstein, L., Louie, A., Mier, J.W., and Gucalp, R. (1993). Randomized phase II trial of high-dose interleukin-2 either alone or in combination with interferon alfa-2b in advanced renal cell carcinoma. J. Clin. Oncol. *11*, 661–670. https://doi.org/10.1200/JCO.1993.11.4.661.
6. Atkins, M.B., Lotze, M.T., Dutcher, J.P., Fisher, R.I., Weiss, G., Margolin, K., Abrams, J., Sznol, M., Parkinson, D., Hawkins, M., et al. (1999). High-dose recombinant interleukin 2 therapy for patients with metastatic melanoma: analysis of 270 patients treated between 1985 and 1993. J. Clin. Oncol. *17*, 2105–2116. https://doi.org/10.1200/JCO.1999.17.7.2105.
7. Fyfe, G., Fisher, R.I., Rosenberg, S.A., Sznol, M., Parkinson, D.R., and Louie, A.C. (1995). Results of treatment of 255 patients with metastatic renal cell carcinoma who received high-dose recombinant interleukin-2 therapy. J. Clin. Oncol. *13*, 688–696. https://doi.org/10.1200/JCO.1995.13.3.688.
8. Hoyos, V., Savoldo, B., Quintarelli, C., Mahendravada, A., Zhang, M., Vera, J., Heslop, H.E., Rooney, C.M., Brenner, M.K., and Dotti, G. (2010). Engineering CD19-specific T lymphocytes with interleukin-15 and a suicide gene to enhance their anti-lymphoma/leukemia effects and safety. Leukemia *24*, 1160–1170. https://doi.org/10.1038/leu.2010.75.
9. Chen, Y., Sun, C., Landoni, E., Metelitsa, L., Dotti, G., and Savoldo, B. (2019). Eradication of Neuroblastoma by T Cells Redirected with an Optimized GD2-Specific Chimeric Antigen Receptor and Interleukin-15. Clin. Cancer Res. *25*, 2915–2924. https://doi.org/10.1158/1078-0432.CCR-18-1811.
10. Steffin, D., Ghatwai, N., Montalbano, A., Rathi, P., Courtney, A.N., Arnett, A.B., Fleurence, J., Sweidan, R., Wang, T., Zhang, H., et al. (2025). Interleukin-15-armored GPC3-CAR T cells for patients with solid cancers. Nature *637*, 940–946. https://doi.org/10.1038/s41586-024-08261-8.
11. Uslu, U., Castelli, S., and June, C.H. (2024). CAR T cell combination therapies to treat cancer. Cancer Cell *42*, 1319–1325. https://doi.org/10.1016/j.ccell.2024.07.002.
12. Uslu, U., and June, C.H. (2025). Beyond the blood: expanding CAR T cell therapy to solid tumors. Nat. Biotechnol. *43*, 506–515. https://doi.org/10.1038/s41587-024-02446-2.
13. Angkasekwinai, P., and Dong, C. (2021). IL-9-producing T cells: potential players in allergy and cancer. Nat. Rev. Immunol. *21*, 37–48. https://doi.org/10.1038/s41577-020-0396-0.
14. Purwar, R., Schlapbach, C., Xiao, S., Kang, H.S., Elyaman, W., Jiang, X., Jetten, A.M., Khoury, S.J., Fuhlbrigge, R.C., Kuchroo, V.K., et al. (2012). Robust tumor immunity to melanoma mediated by interleukin-9-producing T cells. Nat. Med. *18*, 1248–1253. https://doi.org/10.1038/nm.2856.
15. Lu, Y., Hong, S., Li, H., Park, J., Hong, B., Wang, L., Zheng, Y., Liu, Z., Xu, J., He, J., et al. (2012). Th9 cells promote antitumor immune responses in vivo. J. Clin. Invest. *122*, 4160–4171. https://doi.org/10.1172/JCI65459.
16. Lu, Y., Hong, B., Li, H., Zheng, Y., Zhang, M., Wang, S., Qian, J., and Yi, Q. (2014). Tumor-specific IL-9-producing CD8+ Tc9 cells are superior effector than type-I cytotoxic Tc1 cells for adoptive immunotherapy of cancers. Proc. Natl. Acad. Sci. USA *111*, 2265–2270. https://doi.org/10.1073/pnas.1317431111.
17. Liu, L., Bi, E., Ma, X., Xiong, W., Qian, J., Ye, L., Su, P., Wang, Q., Xiao, L., Yang, M., et al. (2020). Enhanced CAR-T activity against established tumors by polarizing human T cells to secrete interleukin-9. Nat. Commun. *11*, 5902. https://doi.org/10.1038/s41467-020-19672-2.
18. Jiang, H., Limsuwannarot, S., Kulhanek, K.R., Pal, A., Labiad, O., Rysavy, L.W., Wong, A., Su, C., Cavender, S., Soro, J., et al. (2025). IL-9 as a naturally orthogonal cytokine with optimal JAK/STAT signaling for engineered T cell therapy. Immunity. *59*. https://doi.org/10.1016/j.immuni.2025.10.024.
19. Kalbasi, A., Siurala, M., Su, L.L., Tariveranmoshabad, M., Picton, L.K., Ravikumar, P., Li, P., Lin, J.X., Escuin-Ordinas, H., Da, T., et al. (2022). Potentiating adoptive cell therapy using synthetic IL-9 receptors. Nature *607*, 360–365. https://doi.org/10.1038/s41586-022-04801-2.
20. Noelle, R.J., and Nowak, E.C. (2010). Cellular sources and immune functions of interleukin-9. Nat. Rev. Immunol. *10*, 683–687. https://doi.org/10.1038/nri2848.
21. Bakiyeva, L.T., Fau, B.R., Rushton, N., and Rushton, N. (2005). Inter-individual and intra-individual variability in TNF-alpha production by human peripheral blood cells in vitro. Cytokine *30*, 35–40. https://doi.org/10.1016/j.cyto.2004.11.011.
22. Johnson, M.D., Vito, F., and O'Connell, M.J. (2008). Mesothelin expression in the leptomeninges and meningiomas. J. Histochem. Cytochem. *56*, 579–585. https://doi.org/10.1369/jhc.2008.950477.
23. Chakraborty, S., Kubatzky, K.F., and Mitra, D.K. (2019). An Update on Interleukin-9: From Its Cellular Source and Signal Transduction to Its Role in Immunopathogenesis. Int. J. Mol. Sci. *20*, 2113. https://doi.org/10.3390/ijms20092113.
24. Good, C.R., Aznar, M.A., Kuramitsu, S., Samareh, P., Agarwal, S., Donahue, G., Ishiyama, K., Wellhausen, N., Rennels, A.K., Ma, Y., et al. (2021). An NK-like CAR T cell transition in CAR T cell dysfunction. Cell *184*, 6081–6100.e26. https://doi.org/10.1016/j.cell.2021.11.016.
25. Agarwal, S., Aznar, M.A., Rech, A.J., Good, C.R., Kuramitsu, S., Da, T., Gohil, M., Chen, L., Hong, S.A., Ravikumar, P., et al. (2023). Deletion of the inhibitory co-receptor CTLA-4 enhances and invigorates chimeric antigen receptor T cells. Immunity *56*, 2388–2407.e9. https://doi.org/10.1016/j.immuni.2023.09.001.
26. Gizard, F., Lavallée, B., DeWitte, F., and Hum, D.W. (2001). A novel zinc finger protein TReP-132 interacts with CBP/p300 to regulate human CYP11A1 gene expression. J. Biol. Chem. *276*, 33881–33892. https://doi.org/10.1074/jbc.M100113200.
27. Gizard, F., Lavallee, B., DeWitte, F., Teissier, E., Staels, B., and Hum, D.W. (2002). The transcriptional regulating protein of 132 kDa (TReP-132) enhances P450scc gene transcription through interaction with steroidogenic factor-1 in human adrenal cells. J. Biol. Chem. *277*, 39144–39155. https://doi.org/10.1074/jbc.M205786200.
28. Guo, Y., Xie, Y.Q., Gao, M., Zhao, Y., Franco, F., Wenes, M., Siddiqui, I., Bevilacqua, A., Wang, H., Yang, H., et al. (2021). Metabolic reprogramming of terminally exhausted CD8(+) T cells by IL-10 enhances anti-tumor immunity. Nat. Immunol. *22*, 746–756. https://doi.org/10.1038/s41590-021-00940-2.
29. Zhao, Y., Chen, J., Andreatta, M., Feng, B., Xie, Y.Q., Wenes, M., Wang, Y., Gao, M., Hu, X., Romero, P., et al. (2024). IL-10-expressing CAR T cells resist dysfunction and mediate durable clearance of solid tumors and metastases. Nat. Biotechnol. *42*, 1693–1704. https://doi.org/10.1038/s41587-023-02060-8.
30. Perucha, E., Melchiotti, R., Bibby, J.A., Wu, W., Frederiksen, K.S., Roberts, C.A., Hall, Z., LeFriec, G., Robertson, K.A., Lavender, P., et al. (2019). The cholesterol biosynthesis pathway regulates IL-10 expression in human Th1 cells. Nat. Commun. *10*, 498. https://doi.org/10.1038/s41467-019-08332-9.
31. Narayan, V., Barber-Rotenberg, J.S., Jung, I.Y., Lacey, S.F., Rech, A.J., Davis, M.M., Hwang, W.T., Lal, P., Carpenter, E.L., Maude, S.L., et al. (2022). PSMA-targeting TGFbeta-insensitive armored CAR T cells in metastatic castration-resistant prostate cancer: a phase 1 trial. Nat. Med. *28*, 724–734. https://doi.org/10.1038/s41591-022-01726-1.

32. McInnes, L., Healy, J., Saul, N., and Großberger, L. (2018). UMAP: Uniform Manifold Approximation and Projection. J. Open Source Software *3*, 861. https://doi.org/10.21105/joss.00861.

33. Finak, G., McDavid, A., Yajima, M., Deng, J., Gersuk, V., Shalek, A.K., Slichter, C.K., Miller, H.W., McElrath, M.J., Prlic, M., et al. (2015). MAST: a flexible statistical framework for assessing transcriptional changes and characterizing heterogeneity in single-cell RNA sequencing data. Genome Biol. *16*, 278. https://doi.org/10.1186/s13059-015-0844-5.

34. Wherry, E.J., and Kurachi, M. (2015). Molecular and cellular insights into T cell exhaustion. Nat. Rev. Immunol. *15*, 486–499. https://doi.org/10.1038/nri3862.

35. Kuleshov, M.V., Jones, M.R., Rouillard, A.D., Fernandez, N.F., Duan, Q., Wang, Z., Koplev, S., Jenkins, S.L., Jagodnik, K.M., Lachmann, A., et al. (2016). Enrichr: a comprehensive gene set enrichment analysis web server 2016 update. Nucleic Acids Res. *44*, W90–W97. https://doi.org/10.1093/nar/gkw377.

36. Street, K., Risso, D., Fletcher, R.B., Das, D., Ngai, J., Yosef, N., Purdom, E., and Dudoit, S. (2018). Slingshot: cell lineage and pseudotime inference for single-cell transcriptomics. BMC Genomics *19*, 477. https://doi.org/10.1186/s12864-018-4772-0.

37. Gérard, A., van der Kammen, R.A., Janssen, H., Ellenbroek, S.I., and Collard, J.G. (2009). The Rac activator Tiam1 controls efficient T-cell trafficking and route of transendothelial migration. Blood *113*, 6138–6147. https://doi.org/10.1182/blood-2008-07-167668.

38. La Manno, G., Soldatov, R., Zeisel, A., Braun, E., Hochgerner, H., Petukhov, V., Lidschreiber, K., Kastriti, M.E., Lönnerberg, P., Furlan, A., et al. (2018). RNA velocity of single cells. Nature *560*, 494–498. https://doi.org/10.1038/s41586-018-0414-6.

39. Han, H., Cho, J.W., Lee, S., Yun, A., Kim, H., Bae, D., Yang, S., Kim, C.Y., Lee, M., Kim, E., et al. (2018). TRRUST v2: an expanded reference database of human and mouse transcriptional regulatory interactions. Nucleic Acids Res. *46*, D380–D386. https://doi.org/10.1093/nar/gkx1013.

40. Hu, X., and Ivashkiv, L.B. (2009). Cross-regulation of signaling pathways by interferon-gamma: implications for immune responses and autoimmune diseases. Immunity *31*, 539–550. https://doi.org/10.1016/j.immuni.2009.09.002.

41. Kaminskiy, Y., and Melenhorst, J.J. (2022). STAT3 Role in T-Cell Memory Formation. Int. J. Mol. Sci. *23*, 2878. https://doi.org/10.3390/ijms23052878.

42. Rada-Iglesias, A., Ameur, A., Kapranov, P., Enroth, S., Komorowski, J., Gingeras, T.R., and Wadelius, C. (2008). Whole-genome maps of USF1 and USF2 binding and histone H3 acetylation reveal new aspects of promoter structure and candidate genes for common human disorders. Genome Res. *18*, 380–392. https://doi.org/10.1101/gr.6880908.

43. Naukkarinen, J., Gentile, M., Soro-Paavonen, A., Saarela, J., Koistinen, H.A., Pajukanta, P., Taskinen, M.R., and Peltonen, L. (2005). USF1 and dyslipidemias: converging evidence for a functional intronic variant. Hum. Mol. Genet. *14*, 2595–2605. https://doi.org/10.1093/hmg/ddi294.

44. Sung, H., Ferlay, J., Siegel, R.L., Laversanne, M., Soerjomataram, I., Jemal, A., and Bray, F. (2021). Global Cancer Statistics 2020: GLOBOCAN Estimates of Incidence and Mortality Worldwide for 36 Cancers in 185 Countries. CA Cancer J. Clin. *71*, 209–249. https://doi.org/10.3322/caac.21660.

45. Posey, A.D., Jr., Young, R.M., and June, C.H. (2024). Future perspectives on engineered T cells for cancer. Trends Cancer *10*, 687–695. https://doi.org/10.1016/j.trecan.2024.05.007.

46. Fraietta, J.A., Lacey, S.F., Orlando, E.J., Pruteanu-Malinici, I., Gohil, M., Lundh, S., Boesteanu, A.C., Wang, Y., O'Connor, R.S., Hwang, W.T., et al. (2018). Determinants of response and resistance to CD19 chimeric antigen receptor (CAR) T cell therapy of chronic lymphocytic leukemia. Nat. Med. *24*, 563–571. https://doi.org/10.1038/s41591-018-0010-1.

47. Gattinoni, L., Klebanoff, C.A., and Restifo, N.P. (2012). Paths to stemness: building the ultimate antitumour T cell. Nat. Rev. Cancer *12*, 671–684. https://doi.org/10.1038/nrc3322.

48. Bulliard, Y., Andersson, B.S., Baysal, M.A., Damiano, J., and Tsimberidou, A.M. (2023). Reprogramming T cell differentiation and exhaustion in CAR-T cell therapy. J. Hematol. Oncol. *16*, 108. https://doi.org/10.1186/s13045-023-01504-7.

49. Kaplan, M.H., Sun, Y.L., Hoey, T., and Grusby, M.J. (1996). Impaired IL-12 responses and enhanced development of Th2 cells in Stat4-deficient mice. Nature *382*, 174–177. https://doi.org/10.1038/382174a0.

50. Thierfelder, W.E., van Deursen, J.M., Yamamoto, K., Tripp, R.A., Sarawar, S.R., Carson, R.T., Sangster, M.Y., Vignali, D.A., Doherty, P.C., Grosveld, G.C., et al. (1996). Requirement for Stat4 in interleukin-12-mediated responses of natural killer and T cells. Nature *382*, 171–174. https://doi.org/10.1038/382171a0.

51. Radpour, R., Simillion, C., Wang, B., Abbas, H.A., Riether, C., and Ochsenbein, A.F. (2024). IL-9 secreted by leukemia stem cells induces Th1-skewed CD4+ T cells, which promote their expansion. Blood *144*, 888–903. https://doi.org/10.1182/blood.2024024000.

52. Fridman, W.H., Pagès, F., Sautès-Fridman, C., and Galon, J. (2012). The immune contexture in human tumours: impact on clinical outcome. Nat. Rev. Cancer *12*, 298–306. https://doi.org/10.1038/nrc3245.

53. Wang, D., Aguilar, B., Starr, R., Alizadeh, D., Brito, A., Sarkissian, A., Ostberg, J.R., Forman, S.J., and Brown, C.E. (2018). Glioblastoma-targeted CD4+ CAR T cells mediate superior antitumor activity. JCI Insight *3*, e99048. https://doi.org/10.1172/jci.insight.99048.

54. Dillard, P., Köksal, H., Maggadottir, S.M., Winge-Main, A., Pollmann, S., Menard, M., Myhre, M.R., Mælandsmo, G.M., Florenes, V.A., Gaudernack, G., et al. (2021). Targeting Telomerase with an HLA Class II-Restricted TCR for Cancer Immunotherapy. Mol. Ther. *29*, 1199–1213. https://doi.org/10.1016/j.ymthe.2020.11.019.

55. Bai, Z., Feng, B., McClory, S.E., de Oliveira, B.C., Diorio, C., Gregoire, C., Tao, B., Yang, L., Zhao, Z., Peng, L., et al. (2024). Single-cell CAR T atlas reveals type 2 function in 8-year leukaemia remission. Nature *634*, 702–711. https://doi.org/10.1038/s41586-024-07762-w.

56. Villarino, A.V., Kanno, Y., and O'Shea, J.J. (2017). Mechanisms and consequences of Jak-STAT signaling in the immune system. Nat. Immunol. *18*, 374–384. https://doi.org/10.1038/ni.3691.

57. Wingett, S.W., and Andrews, S. (2018). FastQ Screen: A tool for multi-genome mapping and quality control. F1000Research *7*, 1338. https://doi.org/10.12688/f1000research.15931.

58. Zheng, G.X.Y., Terry, J.M., Belgrader, P., Ryvkin, P., Bent, Z.W., Wilson, R., Ziraldo, S.B., Wheeler, T.D., McDermott, G.P., Zhu, J., et al. (2017). Massively parallel digital transcriptional profiling of single cells. Nat. Commun. *8*, 1–12. https://doi.org/10.1038/ncomms14049.

59. Wilson, W.V. (2022). scGEM2Cellr: R Package for Cell Selection from GEM (Gel Bead in Emulsion) Single Cell Fluidic Technologies. Zenodo.

60. McCarthy, D.J., Campbell, K.R., Lun, A.T.L., and Wills, Q.F. (2017). Scater: pre-processing, quality control, normalization and visualization of single-cell RNA-seq data in R. Bioinformatics *33*, 1179–1186. https://doi.org/10.1093/bioinformatics/btw777.

61. Germain, P.L., Lun, A., Garcia Meixide, C., Macnair, W., and Robinson, M.D. (2021). Doublet identification in single-cell sequencing data using scDblFinder. F1000Res *10*, 979. https://doi.org/10.12688/f1000research.73600.2.

62. Korsunsky, I., Millard, N., Fan, J., Slowikowski, K., Zhang, F., Wei, K., Baglaenko, Y., Brenner, M., Loh, P.R., and Raychaudhuri, S. (2019). Fast, sensitive and accurate integration of single-cell data with Harmony. Nat. Methods *16*, 1289–1296. https://doi.org/10.1038/s41592-019-0619-0.

63. Choudhary, S., and Satija, R. (2022). Comparison and evaluation of statistical error models for scRNA-seq. Genome Biol. *23*, 27. https://doi.org/10.1186/s13059-021-02584-9.

64. de Bézieux, H.R., Street, K., Fischer, S., Van den Berge, K., Chance, R., Risso, D., Gillis, J., Ngai, J., Purdom, E., and Dudoit, S. (2020). Improving replicability in single-cell RNA-Seq cell type discovery with Dune. Preprint at bioRxiv. https://doi.org/10.1101/2020.03.03.974220.

65. Van den Berge, K., Roux de Bézieux, H., Street, K., Saelens, W., Cannoodt, R., Saeys, Y., Dudoit, S., and Clement, L. (2020). Trajectory-based differential expression analysis for single-cell sequencing data. Nat. Commun. *11*, 1201. https://doi.org/10.1038/s41467-020-14766-3.

66. Bergen, V., Lange, M., Peidli, S., Wolf, F.A., and Theis, F.J. (2020). Generalizing RNA velocity to transient cell states through dynamical modeling. Nat Biotechnol *38*, 1408–1414. https://doi.org/10.1038/s41587-020-0591-3.

67. Kloss, C.C., Lee, J., Zhang, A., Chen, F., Melenhorst, J.J., Lacey, S.F., Maus, M.V., Fraietta, J.A., Zhao, Y., and June, C.H. (2018). Dominant-Negative TGF-beta Receptor Enhances PSMA-Targeted Human CAR T Cell Proliferation And Augments Prostate Cancer Eradication. Mol. Ther. *26*, 1855–1866. https://doi.org/10.1016/j.ymthe.2018.05.003.

68. Watanabe, K., Luo, Y., Da, T., Guedan, S., Ruella, M., Scholler, J., Keith, B., Young, R.M., Engels, B., Sorsa, S., et al. (2018). Pancreatic cancer therapy with combined mesothelin-redirected chimeric antigen receptor T cells and cytokine-armed oncolytic adenoviruses. JCI Insight *3*, e99573. https://doi.org/10.1172/jci.insight.99573.

69. Kutner, R.H., Zhang, X.Y., and Reiser, J. (2009). Production, concentration and titration of pseudotyped HIV-1-based lentiviral vectors. Nat. Protoc. *4*, 495–505. https://doi.org/10.1038/nprot.2009.22.

70. Hippen, A.A., Falco, M.M., Weber, L.M., Erkan, E.P., Zhang, K., Doherty, J.A., Vähärautio, A., Greene, C.S., and Hicks, S.C. (2021). miQC: An adaptive probabilistic framework for quality control of single-cell RNA-sequencing data. PLOS Comput. Biol. *17*, e1009290. https://doi.org/10.1371/journal.pcbi.1009290.

71. Amezquita, R.A., Lun, A.T.L., Becht, E., Carey, V.J., Carpp, L.N., Geistlinger, L., Marini, F., Rue-Albrecht, K., Risso, D., Soneson, C., et al. (2020). Publisher Correction: Orchestrating single-cell analysis with Bioconductor. Nat. Methods *17*, 242. https://doi.org/10.1038/s41592-019-0700-8.

72. Rozenblatt-Rosen, O., Stubbington, M.J.T., Regev, A., and Teichmann, S.A. (2017). The Human Cell Atlas: from vision to reality. Nature *550*, 451–453. https://doi.org/10.1038/550451a.

73. Chu, Y., Dai, E., Li, Y., Han, G., Pei, G., Ingram, D.R., Thakkar, K., Qin, J.J., Dang, M., Le, X., et al. (2023). Pan-cancer T cell atlas links a cellular stress response state to immunotherapy resistance. Nat. Med. *29*, 1550–1562. https://doi.org/10.1038/s41591-023-02371-y.

74. Sara Aibar, S.A. (2022). AUCell: Analysis of 'gene set' activity in single-cell RNA-seq data (e.g. identify cells with specific gene signatures). Bioconductor Version: Release (3.18). https://doi.org/10.18129/B9.bioc.AUCell.

75. Murphy, A.E., and Skene, N.G. (2022). A balanced measure shows superior performance of pseudobulk methods in single-cell RNA-sequencing analysis. Nat. Commun. *13*, 7851. https://doi.org/10.1038/s41467-022-35519-4.

76. Love, M.I., Huber, W., and Anders, S. (2014). Moderated estimation of fold change and dispersion for RNA-seq data with DESeq2. Genome Biol. *15*, 550. https://doi.org/10.1186/s13059-014-0550-8.

77. Müller-Dott, S., Tsirvouli, E., Vazquez, M., Ramirez Flores, R.O., Badia-I-Mompel, P., Fallegger, R., Türei, D., Lægreid, A., and Saez-Rodriguez, J. (2023). Expanding the coverage of regulons from high-confidence prior knowledge for accurate estimation of transcription factor activities. Nucleic Acids Res. *51*, 10934–10949. https://doi.org/10.1093/nar/gkad841.

78. Agarwal, S., Wellhausen, N., Levine, B.L., and June, C.H. (2021). Production of Human CRISPR-Engineered CAR-T Cells. J. Vis. Exp. *169*. https://doi.org/10.3791/62299.

STAR★METHODS

KEY RESOURCES TABLE

REAGENT or RESOURCE	SOURCE	IDENTIFIER
Antibodies		
anti-mouse CD3	Biolegend	Cat# 100229, RRID: AB_11204249
anti-mouse CD11b	Biolegend	Cat# 101242, RRID: AB_2563310
anti-mouse CD44	Biolegend	Cat# 103030, RRID: AB_830786
anti-mouse CD45	Biolegend	Cat# 103128, RRID: AB_493714
anti-mouse CD62L	Biolegend	Cat# 104406, RRID: AB_313092
anti-mouse CD86	Biolegend	Cat# 105020, RRID: AB_493465
anti-mouse I-A/I-E (MHCII)	Biolegend	Cat# 107636, RRID: AB_2561397
anti-mouse NK1.1	Biolegend	Cat# 108748, RRID: AB_2564219
anti-mouse CD45.1	Biolegend	Cat# 110741, RRID: AB_2563378
anti-mouse CD19	Biolegend	Cat# 115543, RRID: AB_11218994
anti-mouse CD11c	Biolegend	Cat# 117318, RRID: AB_493568
anti-mouse F4/80	Biolegend	Cat# 123128, RRID: AB_893484
anti-mouse Ly6G	Biolegend	Cat# 127626, RRID: AB_2561339
anti-mouse Ly6C	Biolegend	Cat# 128032, RRID: AB_2562177
anti-mouse CD206	Biolegend	Cat# 141706, RRID: AB_10895754
anti-mouse CD95 (Fas)	Biolegend	Cat# 152604, RRID: AB_2632898
anti-mouse CD129 (IL-9R)	Biolegend	Cat# 158704, RRID: AB_2860742
anti-human CD4	Biolegend	Cat# 300558, RRID: AB_2564392
anti-human CD8	Biolegend	Cat# 300934, RRID: AB_2814114
anti-human CD45RA	Biolegend	Cat# 304114, RRID: AB_528816
anti-human CD129 (IL-9R)	Biolegend	Cat# 310404, RRID: AB_314817
anti-human EpCAM	Biolegend	Cat# 324206, RRID: AB_756079
anti-human PD-1	Biolegend	Cat# 329920, RRID: AB_10900818
anti-human TIM3	Biolegend	Cat# 345016, RRID: AB_2561933
anti-human CD27	Biolegend	Cat# 356412, RRID: AB_2562258
anti-human CD45	Biolegend	Cat# 368524, RRID: AB_2715825
anti-human CD45	Biolegend	Cat# 304032, RRID: AB_10900423
anti-human LAG3	eBioscience	Cat# 61-2239-42, RRID: AB_2574595
Phospho-STAT1 (Tyr701) monoclonal antibody	Cell Signaling Technology	Cat# 8062S, RRID: AB_10859888
phospho-STAT3 (pY705) monoclonal antibody	BD Biosciences	Cat# 557815, RRID: AB_647144
phospho-STAT4 (pY693) monoclonal antibody	BD Biosciences	Cat# 561217, RRID: AB_10643004
phospho-STAT5 (pY694) monoclonal antibody	BD Biosciences	Cat# 560117, RRID: AB_1645546
anti-human IgG F(ab')2	Jackson ImmunoResearch	Cat# 109-066-006, RRID: AB_2337634
anti-mouse IgG F(ab')$_2$	Jackson ImmunoResearch	Cat# 115-066-072, RRID: AB_2338583
anti-human TGF-beta RII	R&D systems	Cat# FAB2411A, RRID: AB_10990409
anti-mouse IL-9	Bio X Cell	Cat# BE0181, RRID: AB_10950648
mouse IgG2a isotype control	Bio X Cell	Cat# BE0085, RRID: AB_1107771
anti-human IL-10	Bio X Cell	Cat# BE0441, RRID: AB_2909808
anti-mouse CD3	Bio-rad	Cat# MCA1477T, RRID: AB_10845948
anti-mouse FoxP3	Cell Signaling Technology	Cat# 12653, RRID: AB_2797979
anti-mouse K1rb1c/CD161c	Cell Signaling	Cat# 39197, RRID: AB_2892989

(*Continued on next page*)

Continued

REAGENT or RESOURCE	SOURCE	IDENTIFIER
anti-mouse Pax5	Cell Signaling Technology	Cat# 12709, RRID: AB_2798001
anti-mouse F4/80	Cell Signaling Technology	Cat# 70076, RRID: AB_2799771
anti-mouse CD11c	Cell Signaling Technology	Cat# 97585, RRID: AB_2800282
anti-mouse Ly6G	Cell Signaling Technology	Cat# 87048, RRID: AB_2909808
anti-mouse tryptase	Cell Signaling Technology	Cat# 19523, RRID; AB_2313773
anti-mouse PRG2	Novus Biologicals	Cat# NBP3-04784, RRID: AB_2909808
TruStain FcX (anti-mouse CD16/32) Antibody	Biolegend	Cat# 101320, RRID: AB_1574975
Human TruStain FcX Fc Receptor Blocking Solution	Biolegend	Cat# 422302, RRID: AB_2818986
anti-human STAT4	Cell Signaling Technology	Cat# 2653, RRID: AB_2255156
anti-human GAPDH	Cell Signaling Technology	Cat# 97166, RRID: AB_2756824
anti-mouse 680RD	LI-COR	Cat# 926-68070, RRID: AB_10956588
anti-rabbit 800CW	LI-COR	Cat# 926-32211, RRID: AB_621843
Bacterial and virus strains		
One Shot™ Stbl3™ Chemically Competent E. coli	Invitrogen	Cat# C7373-03
Ad-mIL9	Vector Biolabs	Cat# ADV-262200
Ad-hIL9	Vector Biolabs	Cat# ADV-212216
Ad-GFP	Vector Biolabs	Cat# 1060
Biological samples		
T lymphocytes from human healthy donors	UPenn Human Immunology Core	N/A
Human serum samples from healthy donors	UPenn Human Immunology Core	N/A
Human serum samples from clinical trial participants	University of Pennsylvania/ ClinicalTrials.gov	NCT03323944
Tumor tissue harvested from mice	This paper	N/A
Chemicals, peptides, and recombinant proteins		
Live/Dead Aqua	ThermoFisher	Cat# L34957
Zombie NIR (Biolegend) Fixable Viability Kits	Biolegend	Cat# 423106
CountBright Absolute Counting Beads	ThermoFisher	Cat# C36950
Collagenase/Hyaluronidase	STEMCELL Technologies	Cat# 07912
DNase I Solution (1 mg/mL)	STEMCELL Technologies	Cat# 100-0762
ACK Lysis Buffer	ThermoFisher	Cat# A1049201
Lipofectamine™ 3000 Transfection Reagent	Invitrogen	Cat# L3000001
DNase I from bovine pancreas	Sigma	Cat# 11284932001
EDTA (0.5 M), pH 8.0	Invitrogen	Cat# 15575020
PE Streptavidin	Biolegend	Cat# 405204
APC Streptavidin	Biolegend	Cat# 405207
Bond Polymer Refine Detection kit	Leica	Cat# DS9800
Epitope retrieval BOND ER2 high pH buffer	Leica	Cat# AR9640
IHC/ISH Super Blocking	Leica	Cat# PV6122
ClearVue Mountant	Thermo Scientific	Cat# 4211
Alt-R® Cas9 Electroporation Enhancer, 10 nmol	Integrated DNA technologies	Cat# 1075916
SpyFi Cas9	Aldevron	Cat# 9214
P3 Primary cell 4D-nucleofector X Kit L	Lonza	Cat# V4XP-3024
OpTmizer T Cell Expansion SFM	Gibco	Cat# A1048501
Human AB Serum	GeminiBio	Cat# 100-512
Recombinant Human IL-7	PeproTech	Cat# 200-07

(*Continued on next page*)

Continued

REAGENT or RESOURCE	SOURCE	IDENTIFIER
Recombinant Human IL-15	PeproTech	Cat# 200-15
Animal-Free Recombinant Human IL-9	PeproTech	Cat# AF-200-09
Recombinant Murine IL-9	PeproTech	Cat# 219-19
Recombinant Mouse IL-2	Abcam	Cat# ab9856
Human IL-12 p70 Recombinant Protein	PeproTech	Cat# 200-12H
RetroNectin	Takara	Cat# T100B
4% Formaldehyde Methanol-free	Cell Signaling	Cat# 47746S
Methanol	Cell Signaling	Cat# 13604S
Matrigel	Corning	Cat# CB40234C
CountBright Absolute Counting Beads, (ThermoFisher)	Thermo Fisher	Cat# C36950
LongAmp™ Taq 2X Master Mix	New England Biolabs	Cat# M0287S
RIPA Buffer	Thermo Fisher Scientific	Cat# 89900
Halt™ Protease and Phosphatase Inhibitor Cocktail (100X)	Thermo Fisher Scientific	Cat# 78440
NuPAGE MOPS SDS Running Buffer 20x	Thermo Fisher Scientific	Cat# NP0001
Intercept® (TBS) Blocking Buffer	LI-COR Biosciences	Cat# 927-60003
Critical commercial assays		
Dynabeads™ Human T-Activator CD3/CD28	Gibco	Cat# 40203D
Dynabeads™ Mouse T-Activator CD3/CD28	Gibco	Cat#11452D
QIAGEN Plasmid Plus Maxi Kit	QIAGEN	Cat# 12963
CountBright Absolute Counting Beads, (ThermoFisher)	Thermo Fisher	Cat# C36950
Th1/Th2/Th9/Th17/Th22/Treg Cytokine 17-Plex Mouse ProcartaPlex™ Panel	Invitrogen	Cat# EPX170-26087-901
BD™ Cytometric Bead Array (CBA) Human Th1/Th2/Th17 CBA Kit	BD Biosciences	Cat# 560484
BD™ Cytometric Bead Array (CBA) Human IL-9 Flex Set	BD Biosciences	Cat# 558333
BD™ Cytometric Bead Array (CBA) Human Soluble Protein Master Buffer Kit	BD Biosciences	Cat# 558264
BD™ Cytometric Bead Array (CBA) Mouse IL-9 Flex Set	BD Biosciences	Cat# 558348
BD™ Cytometric Bead Array (CBA) Mouse/ Rat Soluble Protein Master Buffer Kit	BD Biosciences	Cat# 558266
Mouse IL-9 ELISA Kit	Abcam	Cat# ab222505
Human IL-9 ELISA kit	Abcam	Cat# ab242237
EasySep™ Mouse T Cell Isolation Kit	STEMCELL Technologies	Cat# 19851
Vacuum Filter/Storage Systems	Corning	Cat# 430770
Trucount tubes	BD Biosciences	Cat# 340334
NucleoSpin Gel and PCR Clean-up Kit	Macherey-Nagel	Cat# 740609
4%–12% NuPAGE Bis-Tris Gel	Thermo Fisher Scientific	Cat# NP0321BOX
NuPAGE™ Antioxidant	Invitrogen	Cat# NP0005
NuPAGE™ Sample reducing agent (10X)	Invitrogen	Cat# NP0009
iBlot™ 2 Transfer Stacks, PVDF, mini	Thermo Fisher Scientific	Cat# IB24002
Chromium Next GEM Single Cell 5′ Kit v2 Dual Index kit	10x Genomics	Cat# 1000265
Library Construction Kit	10x Genomics	Cat# 1000190
High Sensitivity DNA 5000 ScreenTape	Agilent Technologies	Cat# 5067-5592
KAPA Real-Time PCR Kit	Roche	Cat# 07960204001

(*Continued on next page*)

Continued

REAGENT or RESOURCE	SOURCE	IDENTIFIER
NextSeq 2000 P3 300 Cycle Kit	Illumina	Cat# 20040561
Deposited data		
Raw and analyzed data	This paper	The data discussed in this publication are accessible through GEO Series accession number (https://www.ncbi.nlm.nih.gov/geo/query/acc.cgi?acc=GSE303144) GSE303144
Experimental models: Cell lines		
Human (female) HEK293T	ATCC	CRL-11268, RRID: CVCL_0063
Human (female) AsPC-1	ATCC	CRL-1682, RRID: CVCL_0152
Human (female) AsPC-1 MSLN KO	Laboratory of Carl June	N/A
Human (male) PC3-PSMA	Laboratory of Carl June	N/A
Murine PDA7940b	Laboratory of Gregory Beatty	N/A
Experimental models: Organisms/strains		
NOD/scid/IL2r$\gamma^{-/-}$ (NSG)	Jackson Laboratory	Strain#: 005557, RRID: IMSR_JAX:005557
C57BL/6J	Jackson Laboratory	Strain#: 000664; RRID: IMSR_JAX:000664
B6.SJL-Ptprca Pepcb/BoyJ	Jackson Laboratory	Strain#: 002014, RRID: IMSR_JAX:002014
Oligonucleotides		
STAT4 sgRNA #1: 5'-TTGAAGAAGAA TCGTTGCCA-3'	Integrated DNA Technologies	N/A
STAT4 sgRNA #2: 5'-TTAGATTGTGTA TCAAGAGT-3'	Integrated DNA Technologies	N/A
PCR primer STAT4_Fwd: AGAGACAAA GGCAAGGGAGG	Integrated DNA Technologies	N/A
PCR primer STAT4_Rev: ACCATTTTA CCTTCCCACCAGC	Integrated DNA Technologies	N/A
Sequencing primer 1: GATACATG CAAGTCCCACATGC	Integrated DNA Technologies	N/A
Sequencing primer 2: GCACAATTTCTCTG TATCCTCACC	Integrated DNA Technologies	N/A
Recombinant DNA		
pTRPE M5 CAR BBz	This paper	N/A
pTRPE A03 CAR BBz	This paper	N/A
pTRPE M5 CAR BBz-IL9R	This paper	N/A
pTRPE A03 CAR BBz-IL9R	This paper	N/A
pTRPE dnTGFbRII-PSMA CAR BBz	This paper	N/A
pTRPE dnTGFbRII-PSMA CAR BBz-IL9R	This paper	N/A
Software and algorithms		
FlowJo™ v10.10 Software	BD Life Sciences	https://www.flowjo.com, RRID: SCR_008520
Ingenuity Pathway Analysis Software	QIAGEN	https://digitalinsights.qiagen.com/products-overview/discovery-insights-portfolio/analysis-and-visualization/qiagen-ipa/, RRID: SCR_008653
GraphPad Prism version 10	GraphPad	https://www.graphpad.com/scientific-software/prism/, RRID: SCR_002798
Synthego ICE	Synthego Corporation	https://ice.synthego.com/
FASTQC (v 0.11.9)	Wingett and Andrews[57]	https://www.bioinformatics.babraham.ac.uk/
FASTQ Screen (v 0.14.0)	Wingett and Andrews[57]	https://www.bioinformatics.babraham.ac.uk/
CellRanger v7.2.0	Zheng et al.[58]	https://www.10xgenomics.com/

(*Continued on next page*)

Continued

REAGENT or RESOURCE	SOURCE	IDENTIFIER
scGEM2Cellr v1	Wilson[59]	https://bioconductor.org/
Scater	McCarthy et al.[60]	https://bioconductor.org/
scDblFinder	Germain et al.[61]	https://bioconductor.org/
Harmony	Korsunsky et al.[62]	https://bioconductor.org/
sctransform v2	Choudhary and Satija[63]	https://bioconductor.org/
Dune	de Bézieux et al.[64]	https://bioconductor.org/
MAST	Finak et al.[33]	https://bioconductor.org/
EnrichR	Kuleshov et al.[35]	N/A
Slingshot	Street et al.[36]	https://bioconductor.org/
tradeSeq	Van den Berge et al.[65]	https://bioconductor.org/
scVelo	Bergen et al.[66]	https://www.helmholtz-munich.de/en/icb/research-groups/theis-lab
Python 3.13	PIP	https://www.python.org/
R 4.3	CRAN	https://www.r-project.org/
Other		
BioRender illustration design tool	BioRender	https://biorender.com/, RRID:SCR_018361

EXPERIMENTAL MODEL AND STUDY PARTICIPANT DETAILS

Cell lines

The murine pancreatic ductal adenocarcinoma (PDAC) cell line PDA7940b was derived from the $Kras^{LSL.G12D/+}p53^{R172H/+}$ (KPC) mouse pancreatic tumor model and was generously provided by Dr. Gregory Beatty from the University of Pennsylvania. PDA7940b cells were cultured in R10 media, comprising RPMI 1640 (Gibco) supplemented with 10% heat-inactivated fetal bovine serum (FBS, Seradigm), 2% 1 M HEPES buffer solution (Gibco), 1% 100X glutaMAX (Gibco), and 1% 10,000 U/mL penicillin and 10,000 μg/mL streptomycin (Gibco). Cells were routinely tested for mycoplasma contamination by the Department of Genetics at the University of Pennsylvania using the MycoAlert Mycoplasma Detection Kit (Lonza).

The human PDA cell line AsPC-1 and the human prostate cancer cell line PC3 were sourced from the American Type Culture Collection (ATCC). AsPC-1 mesothelin (MSLN)-deleted (MSLN-del) cells were generated by CRISPR-Cas9 technology, using Aldevron's SpyFi™ Cas9 nuclease and sgRNA procured from Integrated DNA Technologies. The MSLN-deleted cells underwent three rounds of sorting using FACSAria™ Fusion Sorter (BD Biosciences). The PC3 cell line was genetically modified to express the PSMA protein, click beetle green luciferase, and green fluorescent protein (GFP) followed by purification, as previously described.[67] AsPC-1 WT and MSLN-del cells were cultured in in D20 medium, consisting of Dulbecco's modified Eagle's medium (DMEM) (1X, Gibco) supplemented with 20% heat-inactivated fetal bovine serum (FBS, Seradigm), 2% 1 M HEPES buffer solution (Gibco), 1% 100X glutaMAX (Gibco), and 1% 10,000 U/ml penicillin and 10,000 μg/ml streptomycin (Gibco). Modified PC3 cells were cultured in D10 medium, consisting of DMEM (1X, Gibco) supplemented with 10% FBS (Seradigm), 2% 1 M HEPES buffer solution (Gibco), and 1% 10,000 U/ml penicillin and 10,000 μg/ml streptomycin (Gibco). All cell lines were regularly authenticated by the University of Arizona Genetics Core and were routinely tested for mycoplasma contamination by the Department of Genetics at the University of Pennsylvania using the MycoAlert Mycoplasma Detection Kit (Lonza).

Mice

All animal experiments were approved by the Institutional Animal Care and Use Committee (IACUC) at the University of Pennsylvania (protocol number: 804226), and procedures were carried out in compliance with federal and institutional IACUC guidelines. Age and sex-matched animals were randomly assigned to experimental groups; no gender-specific influences were detected in the experimental results. NOD/scid/IL2r$\gamma^{-/-}$ (NSG) mice were initially obtained from Jackson Laboratories and subsequently bred at the Stem Cell & Xenograft Core (SCXC) at the University of Pennsylvania. For syngeneic mouse studies, C57BL/6 and B6.SJL-$Ptprc^{a}$ $Pepc^{b}$/BoyJ mice were sourced from Jackson Laboratories. Male (NSG) and female (NSG, C57BL/6 and B6.SJL-Ptprca Pepcb/BoyJ) mice, aged six to eight weeks, were used for *in vivo* experiments and maintained in pathogen-free conditions. Schematics of the mouse models employed are provided in both main text and supplementary figures.

Tumor sizes were measured one day prior to treatment to calculate initial tumor volumes, and mice were grouped into cohorts with comparable average tumor sizes. Animals with abnormally fast or slow tumor growth were excluded before treatment. Data were analyzed based on measurable outcomes without blinding. Mice underwent regular veterinary monitoring for signs of illness and were euthanized either at the end of the study or upon reaching pre-established IACUC rodent health endpoints. At no point did tumors exceed the maximum permissible diameter of 2 cm, as set by the institutional review board.

Human Samples

Healthy donor primary T lymphocytes were provided by the University of Pennsylvania Human Immunology Core. Samples are de-identified for compliance with HIPAA rules. Donor sex and age is shown below: ND552 (female, age 29), ND541 (female, age 31), TMP489 (female, age 23), ND627 (male, age 30), ND623 (female, age 25), ND650 (Female, 26), ND307 (Male, 52).

Frozen serum samples were collected from healthy donors and provided by the University of Pennsylvania Human Immunology Core or from pancreatic cancer patients who enrolled in a clinical trial of human mesothelin-targeted (M5) CAR T cell therapy. Patients enrolled in this trial were adults aged 18 years or older with histologically confirmed unresectable or metastatic pancreatic adenocarcinoma. All patients gave informed consent in accordance with the Declaration of Helsinki. This study was registered at ClinicalTrials.gov (identifier NCT03323944).

METHOD DETAILS

General cell culture

The murine pancreatic ductal adenocarcinoma (PDAC) cell line PDA7940b was derived from the $Kras^{LSL.G12D/+}p53^{R172H/+}$ (KPC) mouse pancreatic tumor model and was generously provided by Dr. Gregory Beatty from the University of Pennsylvania. PDA7940b cells were cultured in R10 media, comprising RPMI 1640 (Gibco) supplemented with 10% heat-inactivated fetal bovine serum (FBS, Seradigm), 2% 1 M HEPES buffer solution (Gibco), 1% 100X GlutaMAX (Gibco), and 1% 10,000 U/ml penicillin and 10,000 μg/ml streptomycin (Gibco). Cells were routinely tested for mycoplasma contamination by the Department of Genetics at the University of Pennsylvania using the MycoAlert Mycoplasma Detection Kit (Lonza).

The human PDAC cell line AsPC-1 and the human prostate cancer cell line PC3 were sourced from the American Type Culture Collection (ATCC). AsPC-1 MSLN-deleted (MSLN-del) cells were generated by CRISPR-Cas9 technology, using Aldevron's SpyFi™ Cas9 nuclease and sgRNA procured from Integrated DNA Technologies. The MSLN-deleted cells underwent three rounds of sorting using FACSAria™ Fusion Sorter (BD Biosciences). The PC3 cell line was genetically modified to express the PSMA protein, click beetle green luciferase, and green fluorescent protein (GFP) followed by purification, as previously described.[67] AsPC-1 WT and MSLN-del cells were cultured in D20 medium, consisting of Dulbecco's modified Eagle's medium (DMEM) (1X, Gibco) supplemented with 20% heat-inactivated fetal bovine serum (FBS, Seradigm), 2% 1 M HEPES buffer solution (Gibco), 1% 100X GlutaMAX (Gibco), and 1% 10,000 U/ml penicillin and 10,000 μg/ml streptomycin (Gibco). Modified PC3 cells were cultured in D10 medium, consisting of DMEM (1X, Gibco) supplemented with 10% FBS (Seradigm), 2% 1 M HEPES buffer solution (Gibco), and 1% 10,000 U/ml penicillin and 10,000 μg/ml streptomycin (Gibco). All cell lines were regularly authenticated by the University of Arizona Genetics Core and were routinely tested for mycoplasma contamination by the Department of Genetics at the University of Pennsylvania using the MycoAlert Mycoplasma Detection Kit (Lonza).

Murine CAR T cell production

Retroviral transduction of mouse CAR T cells was previously described.[68] Briefly, spleens from $CD45.1^+$ B6.SJL-Ptprca Pepcb/BoyJ mice were harvested, and T cells were purified with mouse T cell isolation beads (STEMCELL Technologies). T cells were activated with mouse CD3/CD28 Dynabeads (Gibco) at a bead-to-T cell ratio of 2:1. After 48 hours, T cells were transduced with retroviral vectors encoding the anti-mesothelin CAR (A03 CAR) or A03 CAR and IL-9R on recombinant human fibronectin-coated plates (RetroNectin, Takara Bio). Cells were cultured in mouse T cell media consisting of RPMI 1640 (Gibco) supplemented with 10% heat-inactivated FBS (Seradigm), 1% 100X GlutaMAX (Gibco), 1% 10,000 U/mL penicillin + 10,000 ug/mL streptomycin (Gibco), 1X 100 mM sodium pyruvate (Gibco), and 50 uM β-mercaptoethanol (Gibco) supplemented with recombinant mouse IL-2 (Abcam) (50 U/mL). At day five after stimulation, mouse CAR T cells were harvested, de-beaded, and used for *in vitro/in vivo* experiments. To account for differences in CAR surface expression resulting from the larger size of the A03-IL9R construct, all *in vitro* and *in vivo* experiments were performed using equivalent numbers of live CAR^+ T cells across groups, based on flow cytometric detection.

Human CAR T cell production

Lentiviral vectors and human CAR T cells were generated as previously described.[69] Human CAR T cells were produced using T cells from healthy donors obtained from the Human Immunology Core (HIC) at the University of Pennsylvania. For the production of CAR T cells targeting mesothelin, freshly isolated $CD4^+$ and $CD8^+$ T cells were mixed in a 1:1 ratio and activated with human CD3/CD28 Dynabeads (Gibco) at a bead-to-cell ratio of 3:1. Twenty-four hours later, T cells were transduced with lentiviral vectors encoding the anti-mesothelin M5 CAR, M5 CAR and IL-9R, dominant negative TGF-bRII (dnTGF-bRII) and anti-PSMA CAR (Pbbz), or dn-TGFbRII-PBBz and IL-9R, using a multiplicity of infection (MOI) of 3. On day five, the CD3/CD28 beads were removed from the culture. T cells were maintained in R10 media and cultured at a density of 0.8×10^6 cells per mL until they reached a resting state, as determined by cell volume of ~350 fL using a Multisizer 4 Coulter Counter (Beckman). For cryopreservation of T cells, freezing media consisting of 90% heat-inactivated FBS (Seradigm) and 10% dimethyl sulfoxide (DMSO, Sigma-Aldrich) was used.

Phosphoflow signaling assay

Mouse T cells were starved overnight in mouse T cell media without IL-2. Human T cells were starved for 4 hours in RPMI 1640 (Gibco) containing 0.1% FBS (Seradigm). Cells were then stimulated by adding recombinant mouse IL-9 or animal-free human IL-9 (Peprotech) and incubated for 20 minutes at 37°C. In some experiments, human IL-12 (Peprotech) was used as a positive control.

To terminate the reaction, cells were fixed with 1.5% formaldehyde (Cell Signaling Technology) for 15 minutes at room temperature with agitation. For analysis of STAT signaling after repeated antigen stimulation, cells were harvested after our *in vitro* dysfunction model as described below followed by fixation. After fixation, cells were washed with 1X DPBS (Gibco) and then permeabilized using ice-cold 100% methanol (Cell Signaling Technology) for 1 hour on ice. Post-permeabilization, cells were washed with buffer consisting of 1X DPBS (Gibco), 0.5% heat-inactivated FBS (Seradigm), 2.5 mM EDTA (Invitrogen) and 1% 10,000 U/mL penicillin + 10,000 μg/mL streptomycin (Gibco). Cells were subsequently stained for 1 hour at 4°C in the dark with antibodies targeting phospho-STAT1 (Tyr701) (Cell signaling, 8062S), phospho-STAT3 (pY705) (BD Biosciences, 557815), phospho-STAT4 (pY693) (BD Biosciences, 561217) and phospho-STAT5 (pY694) (BD Biosciences, 560117). The stained cells were washed again and analyzed using an LSRFortessa cytometer (BD Biosciences). The data were represented as log fold change of mean fluorescence intensity (MFI), and the results were fitted to a log(agonist) versus dose-response model using Prism 10 software (GraphPad).

CAR T cell *in vitro* dysfunction model

AsPC-1 cells were routinely seeded in 12-well plates at a density of 0.1 x 10^6 cells per well the day before introducing T cells. CAR T cells were thawed in R10 medium and allowed to rest overnight. After 24 hours, T cells were counted, and transduction efficiency was assessed by flow cytometry. Cell viability was determined using a Countess automated cell counter (ThermoFisher Scientific). 0.1 x 10°6 viable CAR T cells per well were then added to the AsPC-1-coated plates. After a 2-day co-culture period, the cells were thoroughly resuspended by frequent pipetting. The resulting cell suspension was centrifuged, and the supernatant (conditioned media) was collected and filtered using a 0.45 μm filter (Corning). The cell pellet was resuspended in a mixture of conditioned media and fresh R10 medium in equal proportions. The T cell suspension was then transferred back to the AsPC-1-coated plates for continued co-culture. This process was repeated every 2 days for a total duration of 10 days. For the IL-9-treated group, animal-free human IL-9 (10 nM, Peprotech) was added starting at the beginning of the assay and every other day. Flow cytometry analysis was performed on Day 0 and 10 for T cell immunophenotyping. For scRNA-seq analysis, live, $EpCAM^-$, $CD45^+$ T cells were sorted as described below.

Cytokine production assays

For cytokine secretion analysis with mouse T cells, cells were incubated in mouse T cell media with or without murine IL-9 (100 nM, Peprotech) for 48 hours, and the resulting cell supernatants were submitted to the Human Immunology Core (HIC) at the University of Pennsylvania for analysis using a Luminex assay. The Th1/Th2/Th9/Th17/Th22/Treg Cytokine 17-Plex Mouse ProcartaPlex™ Panel (Invitrogen) was used to detect mouse cytokines.

For human T cell cytokine secretion analysis, CAR T cells were thawed and incubated in R10 media supplemented with animal-free human IL-9 (10 nM, Peprotech) or without IL-9 (Mock) for 24 hours. The supernatants were then collected and analyzed using the Human Th1/Th2/Th17 Cytokine CBA Kit (BD Biosciences), following the manufacturer's instructions. Sample data were acquired using a FACSymphony A5 flow cytometer (BD Biosciences) equipped with FACSDiva software, and the results were processed using BD CBA Analysis Software (BD Biosciences).

For cytokine secretion analysis following the *in vitro* dysfunction model, human CAR T cells were co-cultured overnight with AsPC-1 cells at a 1:1 effector-to-target cell ratio, or with media as a control. Cytokine concentrations in the supernatants were determined using the Human Th1/Th2/Th17 Cytokine CBA Kit (BD Biosciences), as per the manufacturer's instructions. Sample data were acquired using a FACSymphony A5 flow cytometer (BD Biosciences) equipped with FACSDiva software, and the results were processed using BD CBA Analysis Software (BD Biosciences).

To measure IL-9 production following Ad-mIL9 or Ad-hIL9 infection of tumor cells *in vitro*, PDA7940b or AsPC-1 cells were cultured with Ad-mIL9 or Ad-hIL9 (100 VP/cell) respectively, or with media as a control (Mock). Supernatants were collected at various timepoints, and IL-9 concentrations were assessed using murine or human IL-9 ELISA kits (Abcam). Absorbance readings were obtained using a Synergy H4 plate reader (BioTek).

For the detection of IL-9 in human serum, samples from healthy donors, provided by the Human Immunology Core (HIC) at the University of Pennsylvania, or from patients in clinical trial UPCC14217 (NCT03323944, see Table S1 for sample IDs) provided by the Translational and Correlative Studies Laboratory (TCSL) were analyzed. IL-9 concentrations were determined using a human IL-9 ELISA kit (Abcam, minimal detectable dose 2.3 pg/mL), and the readings were taken on a Synergy H4 plate reader (BioTek).

In vitro cytotoxicity assays

In vitro analysis of CAR T cell killing was performed using a real-time, impedance-based assay with xCELLigence Real-Time Cell Analyzer System (Agilent). Briefly, 10,000 PDA7940b cells, AsPC-1 WT cells or AsPC-1 MSLN-del cells were seeded to a 96-well E-plate. After 24 hours, CAR T cells were added to the wells in different effector-to-target cell (E:T) ratios as indicated for each assay. For experiments with murine CAR T cells, cells were incubated in mouse T cell media with or without IL-9 (100 nM) for 48 hours prior to addition into xCELLigence plates. Tumor killing was monitored every 20 minutes over a total of 5 days. For data analysis, cell counts were normalized to the time point of CAR T cell addition.

Xenograft animal models

For xenograft flank tumor models, AsPC-1 or PC3-PSMA cells were utilized to establish tumors. A total of 2 x 10°6 AsPC-1 cells or 1 x 10°6 PC3-PSMA cells, suspended in 100 μL of a 1:1 mix of Matrigel (Corning) and 1X DPBS (Gibco), were implanted subcutaneously into the right flank of NSG mice. Tumor growth was monitored until it reached a volume of approximately 150-200 mm^3. After 15 days,

mice received an intratumoral (IT) injection of 1 x 10^9 viral particles (VP) of Ad-hIL9 (Vector Biolabs) in 50 μL 1X DPBS. The following day, mice were treated with either 0.03 x 10^6 or 1 x 10^6 CAR T cells, depending on their assigned treatment group. A second dose of Ad-hIL9 (1 x 10^9 VP in 50 μL) was administered via IT injection three days later. Control groups received either Ad-hIL9 alone, CAR T cells alone, or no treatment. For groups not receiving Ad-hIL9, an IT injection of 1X DPBS was given as a control. For the dose titration experiment, mice received doses of 0.03 x 10^6, 0.1 x 10^6, 0.3 x 10^6 or 1 x 10^6 CAR-IL9R T cells in combination with Ad-hIL9. Control groups received either Ad-hIL9 alone or no treatment. For the tumor re-challenge experiment, mice were implanted with 2 x 10^6 AsPC-1 cells by SC injection into the left flank, and treatment-naïve mice were used as a control. In the xenograft prostate cancer model, one cage of mice (from the group treated with CAR T 0.03E6) was flooded on day 67, leading to the removal of this cage from the survival data analysis.

In antibody neutralization experiments, mice received intraperitoneal (IP) injections of either 300 μg of anti-murine IL-9 antibody (BioXcell, BE0181), 300 μg of isotype control antibody (BioXcell, BE0085), or 500 μg of anti-human IL-10 antibody (BioXcell, BE0441) diluted in 1X DPBS starting on the day of the first IT injection and continuing every 3 days.

Tumor size and mouse body weight were measured at least once a week, with values normalized to the day of the first IT injection for analysis presented in the main and supplementary figures. In a separate experiment, NSG mice were sacrificed on day 25 post-treatment for staining of human $CD45^+$ cells in tumor tissues and peripheral blood. Health assessments were conducted following IACUC's body condition scoring (BCS) guidelines.

Syngeneic animal model

C57BL/6 mice were subcutaneously injected with 5 x 10^5 PDA7940b tumor cells in 100 μL of 1X DPBS (Gibco) into the right flank. On day six, mice underwent lymphodepletion via intraperitoneal injection of cyclophosphamide (120 mg/kg, Sigma-Aldrich). The following day, when tumors reached a size of approximately 50-100 mm^3, an intratumoral (IT) injection of Ad-mIL9 (Vector Biolabs) at a dose of 1 x 10^9 VP in 50 μL 1X DPBS was administered. On the next day, 5 x 10^6 viable CAR T cells were injected intravenously (IV) in 150 μL of PBS. To sustain local IL-9 expression over the course of the experiment, a second IT injection of Ad-mIL9 (same dose) was given three days after CAR T cell infusion. Because the adenovirus used in this study is replication-deficient, repeated administration was required to maintain cytokine production within the TME.

A second CAR T cell dose (5 x 10^6 cells) was administered one week after the initial dose, with additional Ad-mIL9 injections given one day before and three days after the second T cell transfer. Control groups received either CAR T cells or Ad-mIL9 alone. For groups not receiving Ad-mIL9, an IT injection of PBS was administered as a control.

An independent replicate was performed to include additional control groups: CAR + Ad-mIL9, CAR-IL9R + Ad-GFP, and Ad-GFP alone. For Ad-GFP treatment groups, mice received IT injections of Ad-GFP (Vector Biolabs) at a dose of 1 × 10^9 VP in 50 μL of 1× DPBS, following the same injection schedule as the Ad-mIL9 groups.

Tumor size and body weight were measured at least twice weekly using calipers, and data were normalized to the day of the first IT injection in the main and supplementary figures where applicable. In specific experiments, mice were sacrificed on day 5 or 6 post-treatment for several analyses: (i) flow cytometry to assess the numbers of CAR T cells and other immune cells in tumors, spleens, and peripheral blood, (ii) pathological assessment and immunohistochemistry (IHC) and (iii) cytokine analysis from mouse serum. Health monitoring was conducted according to the Institutional Animal Care and Use Committee (IACUC) body condition scoring (BCS) guidelines.

Caliper measurements of subcutaneous tumors

Tumor size was measured using calipers, and volumes were calculated with the formula: volume = (length in mm × $width^2$ in mm) / 2. Tumor size values were normalized to the day of the first IT injection in the main and supplementary figures where indicated.

Processing of tumors and spleens

Tumors and spleens were collected and processed into single-cell suspensions as previously detailed.[19] Briefly, after harvesting, tumor tissue was finely chopped into small pieces (3-5 mm) using a scalpel. The fragments were digested in DMEM (Gibco) containing Collagenase/Hyaluronidase (STEMCELL Technologies) and DNase I (1 mg/mL, STEMCELL Technologies) at 37°C while shaking at 200 rpm for 30 minutes. To remove red blood cells, ACK Lysis Buffer (Life Technologies) was applied. Cells were then stained for flow cytometry analysis. For spleens, tissue was gently mashed using the flat end of a syringe plunger, and red blood cells were lysed with ACK Lysis Buffer for subsequent flow cytometry staining and analysis.

Peripheral blood (CAR) T cell analysis

Peripheral blood was collected from C57BL/6 or NSG mice via cardiac puncture for terminal studies or retroorbital bleeding in overall survival studies. Samples were stained and quantified using TruCount tubes (BD Biosciences) as per the manufacturer's guidelines. Data acquisition was performed on an LSRFortessa cytometer (BD Biosciences) equipped with FACSDiva software (BD Biosciences). Data were processed and analyzed using FlowJo version 10 software (BD Biosciences).

Cytokine analysis from mouse serum

To collect serum from C57BL/6 mice, whole blood was obtained via cardiac puncture, allowed to clot at room temperature for 20 minutes, and then centrifuged to separate the serum. Mouse serum was then sent to the Human Immunology Core (HIC) at the

University of Pennsylvania for cytokine analysis using a Luminex assay. The Th1/Th2/Th9/Th17/Th22/Treg Cytokine 17-Plex Mouse ProcartaPlex™ Panel (Invitrogen) was employed to detect various mouse cytokines.

For cytokine analysis in NSG mice, whole blood was obtained via retroorbital bleeding and serum was collected. Serum samples were analyzed using the human IL-9 CBA kit, murine IL-9 CBA kit, or the human Th1/Th2/Th17 Cytokine CBA kit (BD Biosciences), following the manufacturer's instructions. Data acquisition was performed using the FACSymphony A5 flow cytometer (BD Biosciences) with FACSDiva software, and results were analyzed with the BD CBA Analysis Software (BD Biosciences).

Immunohistochemistry (IHC)

Tumors of C57BL/6 mice were harvested and prepared for standard IHC analysis by the Comparative Pathology Core (CPC) at the University of Pennsylvania School of Veterinary Medicine. Formalin fixed tissues were routinely processed for paraffin embedding, sectioning, and staining for hematoxylin and eosin (H&E). For immunohistochemistry, 5 μm thick sections were mounted on ProbeOn™ slides (Thermo Fisher Scientific) and stained using a Leica BOND RXm automated platform combined with the Bond Polymer Refine Detection kit (Leica #DS9800). Briefly, after dewaxing and rehydration, sections were pretreated with the epitope retrieval BOND ER2 high pH buffer (Leica #AR9640) for 20 minutes at 98°C. Endogenous peroxidase was inactivated with 3% hydrogen peroxide for 10 minutes at room temperature (RT). Nonspecific tissue-antibody interactions were blocked with Leica PowerVision IHC/ISH Super Blocking solution (PV6122; Leica Biosystems, Deer Park, IL) for 30 minutes at RT. The same blocking solution also served as diluent for the primary antibodies. A battery of primary antibodies for immune cells were used and included CD3 (Bio-rad, MCA1477T, rat monoclonal antibody, 1/600), FoxP3 (CST, 12653, rabbit monoclonal antibody, 1/300), K1rb1c/CD161c (CST, 39197, rabbit monoclonal antibody, 1/500NK), Pax5 (CST, 12709, rabbit monoclonal antibody, 1/100), F4/80 (CST, 70076, rabbit monoclonal antibody, 1/1000), CD11c (CST, 97585, rabbit monoclonal antibody, 1/150), Ly6G (CST, 87048, rabbit monoclonal antibody, 1/100), tryptase (CST, 19523, rabbit monoclonal antibody, 1/200), and PRG2 (Novus Bio, NBP3-04784, rabbit polyclonal antibody, 1/300). A biotin-free polymeric IHC detection system consisting of horseradish peroxidase (HRP)-conjugated antirabbit or antirat IgG was then applied for 25 minutes at RT. Immunoreactivity was revealed with the diaminobenzidine (DAB) chromogen reaction. Slides were counterstained in hematoxylin, dehydrated in an ethanol series, cleared in xylene, and permanently mounted with a resinous mounting medium (Thermo Scientific ClearVue coverslipper). Slides were then scanned at 20x magnification using the Leica Versa 200 whole slide scanner (Leica Biosystem), visualized and analyzed using the Aperio ImageScope software (Leica Biosystem). For the analysis, nuclear and cytoplasmic cell counting algorithms were used for FoxP3 and PAX5, and for K1RB1C and tryptase, respectively. For cell counting algorithms (PAX5, K1RB1C, FoxP3 and tryptase), the number of positive cells was normalized to the area of analysis on each slide. Positive pixel count algorithms were used for the quantification of area positivity for CD11c, F4/80, Ly6G, and PRG2. For these markers, the positivity was calculated by dividing the number of positive pixels by the total number of pixels in the area of analysis.

Flow cytometry and sorting

For flow cytometry, cells were stained in fluorescence-activated cell sorting (FACS) buffer consisting of 1X DPBS (Gibco), 0.5% heat-inactivated FBS (Seradigm), 2.5 mM EDTA (Invitrogen) and 1% 10,000 U/mL penicillin + 10,000 ug/mL streptomycin (Gibco). For sorting, cells were stained in FACS buffer with 100mg/mL DNase (Sigma-Aldrich). Antibodies specific for human CD4 (300558), CD8 (300934), CD45RA (304114), IL-9R (310404), EpCAM (324206), PD-1 (329920), TIM3 (345016), CD27 (356412) and CD45 (368524/304032) and for mouse CD3 (100229), CD11b (101242), CD44 (103030), CD45 (103128), CD62L (104406), CD86 (105020), MHCII (107636), NK1.1 (108748), CD45.1 (110741), CD19 (115543), CD11c (117318), F4/80 (123128), Ly6G (127626), Ly6C (128032), CD206 (141706), CD95 (152604) and IL-9R (158704) were purchased from Biolegend. Antibodies specific for phospho-STAT3 (pY705) (557815) and phospho-STAT5 (pY694) (560117) were purchased from BD Biosciences. An antibody specific for Phospho-STAT1 (Tyr701) (8062S) was purchased from Cell Signaling. An antibody specific for human LAG3 (61-2239-42) was purchased from eBioscience. An antibody specific for anti-human TGF-beta RII (FAB2411A) was purchased from R&D systems. M5 CAR and A03 CAR expression was assessed using biotinylated goat anti-human IgG F(ab')$_2$ (Jackson ImmunoResearch, 109–066-006) followed by streptavidin (PE- or APC-conjugated, Biolegend). Pbbz expression was assessed using biotinylated goat Anti-Mouse IgG F(ab')$_2$ (Jackson ImmunoResearch, 115-066-072). Live/dead cell staining was performed using a Live/Dead Aqua (Life Technologies) or Zombie NIR (Biolegend) Fixable Viability Kits following manufacturer's protocol. TruStain FcX (anti-mouse CD16/32) Antibody (CAT: 101320; BioLegend) or Human TruStain FcX Fc Receptor Blocking Solution (CAT: 422302; BioLegend) were used prior to staining of single cell suspensions of mouse or human tumors and mouse spleens. CountBright™ Absolute Counting Beads (ThermoFisher) were used as an internal standard according to the manufacturer's instructions to calculate absolute cell counts in cell suspensions. Samples were acquired on an LSRII Fortessa Cytometer (BD Biosciences) or FACSymphony™ A5 SE Cell Analyzer (BD Biosciences) and analyzed with FlowJo v10 software (FlowJo, LLC). Sorting was performed using a FACSAria™ Fusion Sorter (BD Biosciences).

Single-cell RNA sequencing (scRNA-seq)

scRNA-seq was performed by the Genomics Facility at the Wistar Institute. Single cell droplets were generated using the Chromium Next GEM single cell 5' kit v2 Dual Index kit (10x Genomics, Pleasanton, CA). cDNA synthesis and amplification, library preparation and indexing were performed using the 10x Genomics Library Preparation kit (10x Genomics), according to manufacturer's instructions. Overall library size was determined using the Agilent TapeStation 4200 with the High Sensitivity DNA 5000 ScreenTape (Agilent,

Santa Clara, CA) and libraries were quantitated using KAPA real-time PCR (Roche, Wilmington, MA). A total of 9 samples generating 9 libraries were pooled and sequenced on the NextSeq 2000 (Illumina, San Diego, CA) using 2 P3 300 cycle kits (Illumina) resulting in 250 million reads per sample. Run configuration was paired-end with the following parameters: 26 base pair (read1) x 8 base pair (index) x 281 base pair (read2).

scRNA-seq data quality control

Sequencing quality control was conducted with FASTQC (v 0.11.9) and sources of contamination were detected with FASTQ Screen (v 0.14.0). Alignment and quantitation were conducted with CellRanger v7.2.0 using a custom reference genome based on GRCh38 2022 with our CAR sequence inserted. GEM Selection was completed by running the scGEM2Cellr package.[59] Quality control and pre-processing was conducted with the scater package.[60] Doublets were removed using the scDblFinder package.[61] High mitochondrial cells were removed using a linear model of mitochondrial transcript percent by the total genes detected per cell.[70] Genes that were not found in at least 5 cells were discarded. Non-donor-specific variation in the expression of T cell receptor beta variable (TRBV) transcripts induced separation during dimensionality reduction, which was unrelated to the cell types of interest in our study. To address this, we excluded TRAV and TRBV genes from the principal component analysis (PCA) used to generate the Uniform Manifold Approximation and Projection (UMAP). However, these genes were retained for all downstream analyses, including differential gene expression analysis and gene set enrichment analysis.

scRNA-seq data analysis

Data analysis was conducted using the standard Bioconductor analysis approach.[71] Batch effects were assessed using the scater package and addressed using Harmony integration.[60,62] Data normalization was performed using the variance-stabilizing transformation model in sctransform v2.[63] To focus on biological questions, non-biological phenotype clusters caused by T cell variable region transcripts were removed prior to dimensional reduction, which was performed using Uniform Manifold Approximation and Projection (UMAP) with 10 nearest neighbors and a minimum spanning distance of 0.5.[32]

Cluster stability was investigated using adjusted Rand Index and normalized mutual information with the Dune package.[64] Clusters were annotated by scoring cells against the Human Cell Atlas, Pan-Cancer T cell Atlas, and prior publications.[24,72,73] Cell scoring was achieved by calculating the area under the curve for each signature, and clusters were labeled based on a guilt-by-association approach from the cell labels in each cluster.[74] Cluster composition was compared using Welch's t-test.

Differential gene expression was conducted using the MAST package.[33] Gene Set Enrichment Analysis (GSEA) was performed on statistically significant genes using the following databases: MSigDB Hallmark 2020, KEGG 2021 Human, Reactome 2022, GO Biological Process 2023, GO Cellular Component 2023, and GO Molecular Function 2023, implemented with the R package EnrichR.[35]

For pseudobulk analysis, gene counts were calculated by aggregating the expression data from all cells within each group.[75] Differential expression analysis was conducted using a negative binomial generalized linear model, with p-values calculated via the Wald test and adjusted for multiple comparisons using the Benjamini-Hochberg method.[76] Ingenuity Pathway Analysis (IPA, Qiagen Inc.) was utilized to identify differential canonical pathways. For this analysis, differentially expressed genes from the pseudobulk analysis with an adjusted p-value < 0.05 and fold change > 1.5 were included. Top pathways were identified using a z-score > 2, and pathways with a negative z-score were excluded from analysis.

Transcription factor (TF) analysis was performed using the TRRUST v2 database, following a process analogous to GSEA.[39] To validate the most enriched and downregulated TF pathways, we conducted upstream regulator analysis with IPA. Differentially expressed genes from $CD8^+$ or $CD4^+$ CAR^+ cells served as input, with a cutoff of ± 1 $\log_2$ fold change. The top five TFs were selected based on concordance between TRRUST and IPA results, excluding those with z-scores below ± 0.05. The activity of TFs was inferred using a univariate linear model (ULM). This approach utilized the Collection of Transcriptional Regulatory Interactions (CollecTRI) which compiles signed TF-target gene interactions from 12 different resources.[77] The ULM was applied to score the activity of each TF in individual cells.

Trajectory inference was conducted using the slingshot package.[36] Trajectory comparisons were analyzed using the tradeSeq workflow, and genes were identified by fitting a generalized additive model (GAM) for each gene.[65] Donor CAR^+ frequency between conditions of trajectories were determined by Fisher's repeated measures t-test. RNA velocity analysis was performed using the scVelo package. Unless otherwise specified, all scRNA-seq analyses were conducted using Python 3.13 or R 4.3.

CRISPR/Cas9-Mediated STAT4 deletion

CRISPR single-guide RNA (sgRNA) sequences targeting STAT4 were synthesized by Integrated DNA Technologies (IDT). Five sgRNAs were initially screened, and the two with the highest editing efficiency were selected for further experiments. Gene editing, T cell activation, lentiviral transduction, expansion, and validation were performed as previously described.[78] Briefly, $CD4^+$ and $CD8^+$ T cells were mixed at a 1:1 ratio and cultured in OpTmizer T Cell Expansion Medium (Gibco) supplemented with 5 ng/mL each of human IL-7 and IL-15 (PeproTech) (OPT 7/15 medium). After 24 hours, cells were collected and resuspended at 1 x 10°8 cells/mL in P3 electroporation buffer (Lonza). Ribonucleoprotein (RNP) complexes were assembled by incubating sgRNA (5 μg per 10 x 10°6 cells) with recombinant Cas9 protein (Aldevron; 10 μg per 10 x 10°6 cells) for 10 minutes at room temperature. Each RNP complex was supplemented with 16.8 pmol of electroporation enhancer (IDT). T cells were electroporated in 100 μL batches (10 x 10°6 cells) using a 4D-Nucleofector X Unit (Lonza) with program code EH111. Following electroporation, cells were cultured at 5 x 10°6

cells/mL in OPT 7/15 medium. T cell activation was initiated 4-6 hours later using anti-CD3/CD28-coated magnetic beads (Gibco). After 24 hours, T cells were lentivirally transduced with the CAR-IL9R construct and expanded per standard protocol.

Validation of STAT4 deletion

Genomic DNA was extracted, and the target locus was PCR-amplified using LongAmp™ Taq 2X Master Mix (NEB) following the manufacturer's instructions. Amplicons were purified using the NucleoSpin Gel and PCR Clean-up Kit (Macherey-Nagel). Sanger sequencing was performed, and editing efficiency was quantified using the Inference of CRISPR Edits (ICE) tool by Synthego (https://ice.synthego.com/).

STAT4 protein depletion was confirmed by Western blot. Briefly, cells were lysed in RIPA buffer supplemented with protease and phosphatase inhibitors (Thermo Fisher Scientific). Total protein was quantified using a BCA assay (Pierce). Equal amounts of protein were denatured and resolved on a 4–12% NuPAGE Bis-Tris gel (Thermo Fisher Scientific), then transferred to a PVDF membrane using the iBlot2 system (Thermo). Membranes were blocked in Odyssey Blocking Buffer (LI-COR Biosciences) for 1 hour at room temperature and incubated overnight at 4°C with primary antibodies against STAT4 (Cell Signaling Technology, 2653, 1:1000) and GAPDH (Cell Signaling Technology, 97166, 1:1000). After washing, membranes were incubated goat anti-mouse 680RD (926-68070) and goat anti-rabbit 800CW (926-32211) secondary antibodies (LI-COR, 1:10000) for 1 hour. Blots were imaged using the Odyssey CLx Imaging System.

QUANTIFICATION AND STATISTICAL ANALYSIS

Statistical analysis was performed with Prism version 10 (GraphPad). Each figure legend denotes the statistical test used. Survival curves were drawn using the Kaplan-Meier method and the differences of 2 curves were compared with the log-rank Mantel-Cox test. Comparisons between two groups were performed using a two-tailed unpaired Student's t-test. Kruskal-Wallis one-way analysis of variance (ANOVA) was used to compare 3 or more groups. Statistical significance between multiple groups of two variables was assessed by two-way ANOVA with post-hoc tests. For all figures, ns indicates $P > 0.05$ (non-significant), * indicates $P \leq 0.05$, ** indicates $P \leq 0.01$, *** indicates $P \leq 0.001$, and **** indicates $P \leq 0.0001$. Graphs were created by Prism version 10 (GraphPad), Adobe Illustrator (Adobe), and BioRender.com. All *in vitro* data presented are representative of at least two biological replicates. scRNA-seq was performed in three biological replicates (three donors). *In vivo* animal studies were performed using two biological replicates, independently.